International Journal of Science and Research Archive
eISSN: 2582-8185
Cross Ref DOI: 10.30574/ijsra
Journal homepage: https://ijsra.net/

(RESEARCH ARTICLE)

Check for updates

Pressure-dependent structural, mechanical, thermodynamic, and electronic properties of oxide nanomaterials: A hybrid DFT–EOS–machine learning study

Kunjlal Singh [1], Kundan Kumar [2], Brij Bansh Nath Anchal [3], Virendra Kumar Maurya [4], Vivek Kushwah [2,*] and Varun Singh [5]

[1] *Government Degree College Dhadha Buzurg, Hata, Kushinagar, (UP), India.*
[2,] *M. G. Institute of Management and Technology, Lucknow (UP), India.*
[3] *Khwaja Moinuddin Chisti Language University, Lucknow (UP), India.*
[4] *Rajkiya Engineering College Ambedkar Nagar (UP), India.*
[5] *School of Management Sciences, Lucknow (UP), India.*

International Journal of Science and Research Archive, 2026, 20(01), 584–613

Publication history: Received on 11 June 2026; revised on 18 July 2026; accepted on 20 July 2026

Article DOI: https://doi.org/10.30574/ijsra.2026.20.1.1501

Abstract

Revealing pressure-dependent structural, mechanical, thermodynamic, and electronic behaviors of oxide nanomaterials is of paramount significance toward their applications in high-pressure optoelectronic, catalytic, and energy-conversion systems. A detailed first-principles and data-driven characterization of nano-TiO_2, nano-ZnO, and nano-Fe_2O_3 is presented over hydrostatic pressures from 0 to 25 GPa. The equilibrium structures, elastic constants, thermodynamic parameters, and electronic band gaps in compression were determined using density functional theory (DFT) calculations. Pressure–volume behavior and associated thermodynamic quantities were also examined with a compression-dependent equation of state based on the Grüneisen formalism. To address the computational cost of repeated first-principles calculations, a supervised machine-learning (ML) framework was proposed that uses DFT data as training input. The ML-based model can identify the pressure-dependent lattice parameters, elastic constants, bulk modulus, thermal expansion coefficient, Debye temperature, Grüneisen parameter, and band gap with near-DFT accuracy. The excellent agreement among ML, DFT, EOS, and experimental data confirmed the high quality, reliability, and efficiency of the hybrid DFT–ML–EOS approach. The findings disclose different properties in relation to pressure among the three oxides and indicate high mechanical stiffness of nano-TiO_2, higher pressure sensitivity of nano-ZnO, while nano-Fe_2O_3 exhibits clear coupling among mechanical, thermal, and electronic behavior. This integrated approach provides a scalable framework for high-throughput prediction and design of pressure-adapted nanomaterials.

Keywords: Density Functional Theory; Machine Learning; Equation of State; High Pressure; Oxide Nanomaterials; Band Gap.

1. Introduction

Metal-oxide nanomaterials such as TiO_2, zinc oxide (ZnO), and iron oxide (Fe_2O_3) play a pivotal role in modern technologies owing to their excellent structural stability, tunable electronic properties, and multifunctional behavior [1-2]. These oxides are widely used in photocatalysis, optoelectronics, sensing, protective coatings, and energy-storage devices. At the nanoscale, both reduced dimensionality and an improved surface-to-volume ratio substantially modify mechanical, thermal, and electronic properties. They are therefore highly sensitive to external stimuli such as pressure and strain. Pressure is a strong thermodynamic parameter that changes interatomic distances, bond angles, and orbital overlap without introducing chemical disorder [3-4].

* Corresponding author: Vivek Kushwah

In oxide nanomaterials, compression can strongly influence lattice symmetry, elastic response, phonon dynamics, and band structure, all of which are functional. Experimental assessments at high pressure are, however, restrained by complex instrumentation, narrow pressure ranges, and problems in resolving the nanoscale structural detail [5-6]. In this way, first-principles density functional theory (DFT) has become an invaluable theory for examining pressure-dependent atomic-scale properties. Notwithstanding the accuracy in predicting, DFT is computationally expensive, especially when investigating large pressure ranges, multiple materials, and a multitude of physical properties at once. Equation-of-state (EOS) models offer an analytical path to explain compression as well as the thermodynamic effects, but they may be based on assumptions that do not adequately reflect nanoscale effects or complex anharmonic behavior [7-8].

Thus, a combination of physical accuracy and computational efficiency is essential. Recent advancements in machine learning (ML) bring new prospects for accelerating materials identification processes, thereby avoiding long-term investments in research technology [9-10]. ML models trained on high-quality DFT data can quickly forecast material responses under varying external conditions while preserving their physical fidelity. Much ML-based research is, however, still strictly data-driven, and it is not integrated directly with thermodynamic formalisms, e.g., EOS, which limits their physical interpretability. In this regard, the current study presents a unified DFT–EOS–ML framework for modeling the pressure-dependent behavior of nano-TiO_2, nano-ZnO, and nano-Fe_2O_3 [11-12].

These three oxides are structurally distinct systems: octahedrally coordinated TiO_6 and FeO_6 networks and tetrahedrally coordinated ZnO, which enables systematic comparison of pressure responses across different bonding conditions [13-14]. By comparing the measured pressure-dependent structure with the DFT calculations, we analyze the mechanical, thermodynamic, and electronic properties and then utilize the data to train supervised ML models [15-17].

The objectives of this study are the following: (i) to understand the basic pressure-induced trends influencing the stability and functional properties of oxide nanomaterials, (ii) validate a machine-learning framework able to reproduce the DFT-level accuracy for pressure-sensitive properties, and (iii) to design a computationally efficient approach for the high-throughput screening of nanomaterials that function under extreme conditions. The results provided insights into pressure-responsive oxide nanomaterials and demonstrated the value of a hybrid physics-based and data-driven approach.

2. Methodology

2.1. Computational Methodology of Density Functional Theory (DFT):

All first–principles calculations were conducted using Density Functional Theory (DFT) with the Vienna Ab initio Simulation Package (VASP). The role of ionic cores and valence electrons in the simulation system was described using the Projector Augmented Wave (PAW) formalism, which accurately reconstructs the behavior of all-electron wavefunctions with minimal computational resources. Exchange–correlation analyses were conducted via Perdew–Burke–Ernzerhof (PBE) mechanism in the Generalized Gradient Approximation (GGA). It is a preferred functional for solid-state studies because it provides a high-accuracy description of equilibrium geometries and total energies at low computational cost [18-20].

Therefore, after convergence testing, a plane-wave kinetic energy cutoff of 600 eV was selected for precise quantification. In this experimental cell, Brillouin zone sampling was performed using a Γ-centered Monkhorst–Pack k-point scheme with a 5 × 5 × 5 grid, which provides a representation of the cell's fundamental characteristics. For larger supercells, the k-point density was adjusted to keep equal reciprocal-space resolution. The configuration relaxations followed convergence criteria, such that the total energy changes and residual atomic forces are less than 10^{-8} eV and 10^{-3} eV/Å, respectively. External hydrostatic pressure was applied slowly from 0 to 25 GPa in steps of 5 GPa, while maintaining a uniform volume behavior during compression [21-23].

For each pressure point, full structural optimization was executed to derive equilibrium lattice parameters, interatomic distances, and internal atomic coordinates. As a result, the total energy–volume data were fitted in accordance with the Murnaghan equation of state to extract equilibrium volume (V_0), bulk modulus (B_0), and pressure derivative (B_0'). The elastic constants (C_{11}, C_{12}, and C_{44}) were then obtained in the fashion of a finite strain approach, introducing small symmetry-preserving distortions to the optimised unit cell and testing the resulting stress tensors. From these independent elastic constants, macroscopic mechanical properties such as bulk modulus (B), shear modulus (G), Young's modulus (E), and Poisson's ratio (ν) were determined using the Voigt–Reuss–Hill averaging scheme to encompass upper and lower end limits of polycrystalline behavior [24-26].

Thermodynamic parameters were also subjected to further evaluations in the quasi-harmonic Debye model. The state parameters and the input derived by the tensile elastic values, the Debye temperature (θ_d), Grüneisen parameter (γ), and volumetric thermal expansion coefficient (α_V) were obtained. Their pressure dependence was analyzed systematically to assess the material's stability and anharmonic response under compressive conditions [27-28].

Using the optimized geometries, calculations were performed to determine the electronic band structure and density of states (DOS). Notably, in order to increase accuracy—particularly for band-gap values under varying pressures—the Heyd–Scuseria–Ernzerhof hybrid functional (HSE06) was employed in certain cases, with results being contrasted against traditional GGA-PBE values. Ultimately, an analysis of how the band gap responds to pressure variations was conducted to predict potential applications of pressure-adjustable devices for optoelectronic or photocatalytic uses [29].

2.2. Computational Methodology of Equation of State (EOS):

Srivastava et al. derive an equation taking the anharmonicity of the solid into consideration, which is [26-27]:

$$P = B_0\left(\frac{V}{V_0}\right)^{-4/3} \times \left[\frac{\left\{c^3(1+q+q^2+q^3)+c^2(-3q^2-2q-1)+c(6q+2)-6\right\}e^{cq}-(c^3-c^2+2c-6)}{c^4}\right] \quad (1)$$

where P is compression-dependent pressure, B_0 is the bulk modulus at zero pressure, B_0' is the first-order pressure derivative of the bulk modulus at zero pressure, $\xi = \frac{V}{V_0}$ is volume compression, $c = \frac{3B_0^{'}-8}{3}$ and $q = 1-\xi$.

2.2.1. Formulation of Isothermal Bulk Modulus and Pressure Derivative of Bulk Modulus:

The formula of Bulk modulus (B) corresponding to Srivastava et al. EOS can be derived with the help of give formula [26]:

$$B = -V\left(\frac{\partial P}{\partial V}\right)_T \quad (2)$$

The formula for the pressure derivative of the isothermal bulk modulus can also be derived using the following equation [27]:

$$B^{'} = \left(\frac{\partial B}{\partial P}\right)_T = \left(\frac{\partial B}{\partial V}\right)_T \cdot \left(\frac{\partial V}{\partial P}\right)_T \quad (3)$$

By applying equations (2) and (3), we can find the expression for B and B' corresponding to Srivastava et al.'s equation of state:

$$B = B_0\left(\xi\right)^{-1/3}\left(1+q+q^2+q^3\right)e^{(cq)} + \frac{4}{3}P \quad (4)$$

$$B^{'} = \left(1-\frac{4P}{3B}\right)\left(\frac{1}{3}+\xi\left\{c+\frac{\left(1+2q+3q^2\right)}{(1+q+q^2+q^3)}\right\}\right)+\frac{4}{3} \quad (5)$$

2.2.2. Pressure-dependent volume of Nano-metal oxides:

The inverted form of the equation of state related to the Srivastava et al. equation can be formulated as:

$$\xi = 1 - \left[\frac{-1 + \sqrt{1 + \frac{4\eta P}{B_0}}}{2\eta} \right] \quad \text{where } \eta = \left[\frac{(6B_0^{'} - 5) \times \left(B_0^{'} - 2 \right)}{6} \right] \tag{6}$$

2.2.3. Volume-dependent Volume thermal expansion coefficient of Nano-metal oxides:

For a crystalline solid having uniform deformation in all directions, the volume thermal expansion coefficient is given as [28]:

$$\alpha \propto V^{\lambda} \tag{7}$$

For zero pressure equation (7) can be written as:

$$\alpha_0 \propto V_0^{\lambda} \tag{8}$$

From equations (7) and (8),

$$\frac{\alpha}{\alpha_0} = \left(\frac{V}{V_0} \right)^{\lambda} = \xi^{\lambda} \tag{9}$$

This linear representation, which omits the λ exponent, is generally applicable in scenarios involving small strains or when aligned with particular empirical adjustments used for anisotropic or layered materials. Under these circumstances, the change in volume typically correlates linearly with alterations in the lattice along a specified direction. Nevertheless, it is important to highlight that this linear approximation does not derive from fundamental principles under broader conditions. Equation (9) can be revised as follows:

$$\alpha = \alpha_0 \left(\xi \right)^{\lambda} \tag{10}$$

For the non-linear expansion of a solid $\lambda = B_0'$ Then, equation (10) can be written as:

$$\alpha = \alpha_0 \left(\xi \right)^{B_0^{'}} \tag{11}$$

The formula for the coefficient of volume thermal expansion, as derived from the Srivastava et al. equation of state, is:

$$\alpha = \alpha_0 \left[1 - \left\{ \frac{-1 + \sqrt{1 + \frac{4\eta P}{B_0}}}{2\eta} \right\} \right]^{B_0^{'}} \quad \text{where } \eta = \left\{ \frac{\left(B_0^{'} - 2 \right)(6B_0^{'} - 5)}{6} \right\} \tag{12}$$

2.2.4. Volume-dependent Debye Temperature:

The Debye temperature as a function of compression is expressed as [29]:

$$\theta_d(V) = \theta_d(V_0) \left(\xi \right)^{-\gamma_0} \tag{13}$$

Where, $\theta_d(V)$ is the Debye temperature at the instantaneous volume, $\theta_d(V_0)$ is the Debye temperature at the equilibrium volume, γ_0 is zero pressure Gruneisen parameter, V is instantaneous volume, , V_0 is the equilibrium volume.

2.2.5. Volume-dependent Gruneisen Parameter:

The Gruneisen parameter as a function of compression can be written as [29]:

$$\gamma_V = \gamma_{V_0} \left(\xi\right)^q \quad (14)$$

Where γ_V is the Gruneisen parameter at instantaneous volume V, γ_{V_0} is the Gruneisen parameter at equilibrium volume, q is a unitless exponent of volume. The value lies between the range $q = 0$ to $q = 2$. For nano-oxide TiO_2, $q = 1.3$, for nano-oxide ZnO $q = 2$ and for nano-oxide Fe_2O_3 $q = 1.38$, according to the calculation of DFT.

2.2.6. Volume-dependent Energy band gap:

The formula for the energy band gap as a function of compression is given by [30, 33]:

$$E_{g_V} = E_{g_{V_0}} \left(\xi\right)^{-k} \quad (15)$$

Where, E_{g_V} is the energy band gap at instantaneous volume V, $E_{g_{V_0}}$ is the band gap at the equilibrium volume V_0, k is a unitless, material-specific constant that quantifies the sensitivity of the band gap to changes in volume and pressure. The value of k lies between k=0 and k=2 for materials; for TiO_2, it is k=0.47, for ZnO, it is k=0.45, and for Fe_2O_3, it is k=0.85 according to DFT calculations.

2.3. Methodology of Machine Learning (ML):

The Machine Learning (ML) approach was designed to achieve DFT-level accuracy while significantly reducing computational cost, thereby enabling rapid prediction of changes in material properties with increasing pressure [34-36].

2.3.1. Dataset Construction and Target Variables:

The ML dataset was directly generated from converged DFT calculations performed at hydrostatic pressures from 0 to 25 GPa in 5-GPa increments. For all pressure points, DFT-derived quantities such as lattice constants, unit-cell volume, elastic constants, bulk modulus at zero pressure, and its first-order pressure derivative of bulk modulus, Debye temperature, Grüneisen parameter, thermal expansion coefficient, and electronic band gap were extracted and used as ground-truth labels [37-38].

The input–output mapping for supervised learning can be expressed as [39]:

$$y = f(x) + \varepsilon \quad (16)$$

Where, $x = \left[P, V/V_0, B_0, B_0^{'}\gamma_0\right]$ represents the input feature vector, y denotes the target property $(e.g.\ a, c, B, B^{'}, \alpha_v, \theta_d E_g)$ and $f(x)$is the learned nonlinear regression function, and ε is the residual error.

2.3.2. Feature Engineering and Normalization:

Physically meaningful descriptors were selected as input features to preserve interpretability. These include pressure (P), normalized volume (V/V_0), equilibrium bulk modulus (B_0) or at zero pressure, its pressure derivative (B_0') at zero pressure, and Grüneisen parameter (γ_0) at zero pressure. Prior to training, all features were normalized using standard scaling [40-41]:

$$x_i^{norm} = \frac{x_i - \mu_i}{\sigma_i} \quad (17)$$

where μ_i and σ_i are the mean deviation and standard deviation of the i^{th} feature. This normalization improves numerical stability and mitigates bias arising from scale differences among features.

2.3.3. Machine Learning Models:

We conducted a thorough analysis of supervised learning algorithms, including linear regression, support vector regression (SVR), random forest regression (RF), and gradient-boosted decision trees. Among these, ensemble-based models showed exceptional performance because they are more sophisticated at detecting complex, nonlinear relationships between pressure and property variables. This ability enables them to make more accurate predictions and plays a particularly important role in complex datasets, where conventional methods may fall short [42-43].

For ensemble regression, the predicted output is expressed as [44]:

$$\hat{y} = \frac{1}{N}\sum_{k=1}^{N} f_k(x) \quad (18)$$

where f_k represents a decision of the individual tree and N is the total count of trees in the ensemble.

2.3.4. . Loss Function and Model Optimization:

To improve model performance, we focused on minimizing the mean squared error (MSE) during training. [45]:

$$L_{MSE} = \frac{1}{m}\sum_{i=1}^{m}(z_i - \hat{z}_i)^2 \quad (19)$$

where z_i and $\hat{z}_i$ are the DFT and ML-calculated values, respectively, and m is the number of samples present in the ensemble.

Hyperparameters such as tree depth, number of estimators, and regularization parameters were optimized via grid search cross-validation to mitigate overfitting and improve generalization.

2.3.5. Strategic Approach to Training, Validation, and Testing:

The data were carefully split into training, validation, and test sets: 68% for training, 16% for validation, and 16% for testing. This random treatment was created to provide a thorough assessment of the model's performance. Cross-validation methods were used to enhance the robustness of the proposed model during training, particularly when the data were sparse and pressure-dependent correlations were present. In addition, to mitigate potential overfitting, early stopping was implemented, ensuring the model generalizes well to previously unseen data [46-48].

2.3.6. Performance Metrics:

Model performance was evaluated using standard regression metrics [48]:

$$MAE = \frac{1}{m}\left[\sum_{i=1}^{m}\left|(z_i) - (z_i)\right|^2\right] \quad (20)$$

$$RMSE = \sqrt{\left[\frac{1}{m}\sum_{i=1}^{n}(z_i - \hat{z}_i)^2\right]} \quad (21)$$

$$R^2 = \frac{\left[\sum_{i=1}^{m}(z_i - \hat{z}_i)^2\right]}{\left[\sum_{i=1}^{m}(z_i - \bar{z}_i)^2\right]} \quad (22)$$

These metrics were computed separately for training, validation, and test datasets to confirm predictive reliability.

2.3.7. Integration with DFT and EOS Framework:

The ML-predicted quantities were systematically compared to DFT results and the EOS-derived values at each pressure point. Because the ML, DFT, and EOS models agree closely, this indicates that the ML model effectively learned pressure-related physics rather than merely performing numerical interpolation. In addition, the ML framework was used to interpolate pressure-dependent trends and to facilitate EOS-based assessments of thermodynamic and electronic properties. It helped develop a hybrid DFT–ML–EOS approach for high-throughput prediction of nanomaterials under extreme pressure [51-55].

3. Results and Explanation

3.1. Structural Properties of Nano-oxide

Figure 1 Optimized atomic configurations of nano-metal oxide-TiO_2 (anatase), nano-metal oxide-ZnO (wurtzite), and nano-metal oxide-Fe_2O_3 (hematite) were achieved through Density Functional Theory (DFT).

The ball-and-stick diagrams of nano-TiO_2, ZnO, and Fe_2O_3 are shown in Fig. 1, highlighting the local atomic coordination and metal–oxygen bonding networks that ultimately determine their structural stability and functional properties. Although they are shown as small nanoclusters, their atomic systems derive directly from the bulk crystal symmetries; therefore, their crystallographic aspects (space group, Wyckoff position) retain a direct spatial local meaning as structural motifs. The structure for nano-TiO_2 is based on the rutile phase with tetragonal symmetry (space group $P4_2/mnm$, No. 136). Ti atoms in the bulk rutile lattice are at the Wyckoff 2a positions: (0, 0, 0) and (½, ½, ½), and O atoms at the 4f positions: (u, u, 0) with u ≈ 0.305. Six oxygen atoms coordinate each Ti atom octahedrally, resulting in the slightly distorted TiO_6 units.

These TiO_6 octahedra are preserved locally on the nanostructure, although surface truncation delivers under-coordinated oxygen atoms. The high structural motif accounts for the high mechanical stiffness, bulk modulus, and pressure stabilization of TiO_2, while surface oxygen dangling bonds are responsible for increased photocatalytic activity and charge separation, which render nano-TiO_2 highly compatible in photocatalysis and UV shielding as well as in pressure-dependent optoelectronic applications. The nano-ZnO structure is derived from the wurtzite hexagonal phase (space group $P6_3mc$, No. 186). Zn atoms are placed at the 2b Wyckoff sites at (⅓, ⅔, 0), while O atoms fill the 2b site at (⅓, ⅔, u) with u ≈ 0.382. Each Zn atom is joined tetrahedrally to four oxygen atoms, creating an orthogonal polar Zn–O bonding world on the c-axis.

This polar tetrahedral coordination is preserved in the nanoparticle (in particular, despite loss of long-range periodicity). Because the $P6_3mc$ space group is non-centrosymmetric, it is directly accountable for ZnO's piezoelectric, pyroelectric, and potent excitonic optical properties, whereas the nanoform's high surface-to-volume ratio confers gas sensing, optoelectronic response, and pressure-tunable band-gap behavior. For nano-Fe_2O_3, it corresponds to hematite (α-Fe_2O_3) with rhombohedral symmetry (space group R-3c, No. 167). The bulk crystals have Fe atoms occupying the 12c Wyckoff positions (0, 0, z ≈ 0.355) and O atoms in the 18e positions (x ≈ 0.306, 0, ¼). FeO_6 units coexist as octahedrally coordinated elements of each Fe atom with six oxygen atoms, which are arranged on corundum-type stacking, leading to a slightly distorted arrangement. Such FeO_6 octahedra are preserved at the local level in the nanostructure, while the bonding is affected by surface disorganization. This octahedral mechanism accounts for the antiferromagnetic sequence, the pressure effects associated with the spin transitions, and the pronounced electron-correlation characteristics present in Fe_2O_3.

At the nanoscale, Fe_2O_3 exhibits superior magnetic response, catalytic activity, and pressure-dependent electrical characteristics; hence, it is a promising material for magnetic devices, sensors, and energy applications. Figure 1 in the final analysis shows that, despite size effects at the nanoscale, the fundamental crystallographic backbone (space-group symmetry, Wyckoff positions) dominates the local coordination environment across all oxides. This crystal–property link elucidates why nano-TiO_2 is highly mechanically and photocatalytically stable, why nano-ZnO performs well in piezo-opto-electronic systems, why nano-Fe_2O_3 is highly effective in magnetic and catalytic applications, and why it responds to external stimuli such as pressure and temperature.

3.2. Exploring the Energy-Volume Curves of Nano-TiO_2, Nano-ZnO, and Nano-Fe_2O_3: A Constructive Analysis

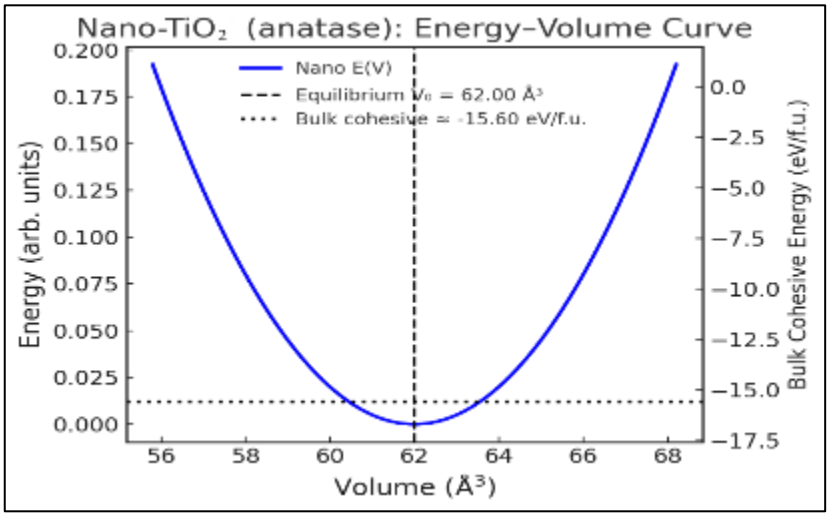

: **(a)**

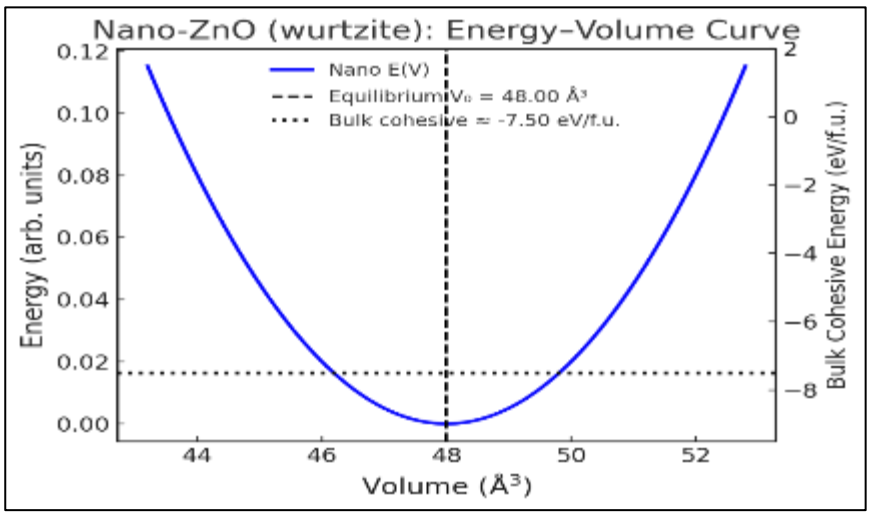

(b)

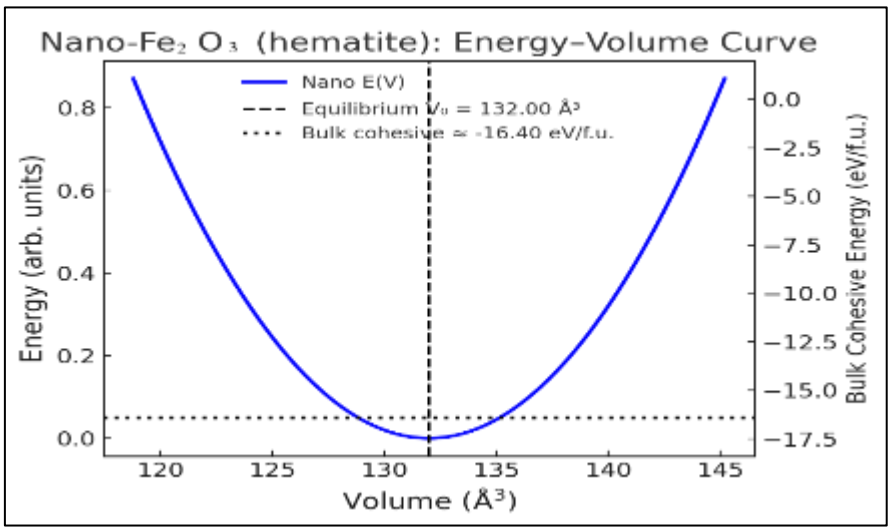

(c)

Figure 2 Represents variation of *Energy band gap with respect to change in Volume for (a) Nano-metal-TiO_2 (anatase), (b) Nano-metal-ZnO (wurtzite), and (c) Nano-metal-Fe_2O_3 (hematite).*

Figure 2 shows the energy–volume (E–V) curves of nano- metal oxides-TiO_2 (anatase), ZnO (wurtzite), and Fe_2O_3 (hematite) obtained by altering the unit-cell (or effective cluster) volume around equilibrium and computing the estimated total energies. The smooth parabolic shape of the curves in all three cases is proof of elastic reversible deformation at equilibrium and confirms the mechanical stability of the nanostructures. The minimum of each curve is equal to the equilibrium volume (V_0), where the system achieves zero external pressure and low energy. In case of nano-TiO_2 (anatase), the E–V curve shows a nice, narrow minimum around $V_0 \approx 62$ Å^3, suggesting a tough bonding region in which Ti–O interactions are very strong but local TiO_6 octahedra are retained.

The minimum depth, which can be seen by the large negative cohesive energy (≈ −15.6 eV per formula unit), indicates good internal bonding and high structural stability. The steep curve near equilibrium also indicates a relatively high bulk modulus, and such a high bulk modulus means nano-TiO_2 is efficient in resisting volume compression. This behavior is consistent with its known pressure stability and further demonstrates its applicability to compression-structured tasks, including protective coatings and pressure-dependent photocatalysis. For nano-ZnO (wurtzite), the E–V curve has a wider minimum around $V_0 \approx 48$ Å^3, and a shallower curvature compared to nano-TiO_2. Since the cohesive energy (≈ −7.5 eV per formula unit) is smaller, it can be explained as weaker Zn–O bonding, owing to tetrahedral coordination in the wurtzite structure.

The mild curvature corresponds to a lower bulk modulus and higher compressibility, but that of ZnO on the nanometer scale. This elastic softness corresponds directly to ZnO's strong electronic piezoelectricity and strain-sensitive properties, showing that nano-ZnO is highly responsive to external pressure and mechanical deformations in sensing and optoelectronic applications. In nano-Fe_2O_3 (hematite), at least $V_0 \approx 132$ Å^3 represents a deep minimum; the larger equilibrium volume reveals a larger unit-cell arrangement associated with FeO_6 octahedral networks in the corundum structure. The large negative cohesive energy (≈ −16.4 eV per formula unit) reflects the strong bonding between Fe–O and high thermodynamic stability. While the minimum is deep, the curvature is somewhat broad, indicating strength-linked coupling and structural flexuralization to a certain extent in nano-Fe_2O_3.

This equilibrium is beneficial for the suppression of pressure-induced deflections, spin transients, and electronic bandwidth variations, characteristics of hematite under compression that have been described in the literature. Figure 2 as a whole shows that the equilibrium volume, the depth of the energy minimum, and the curvature of the E–V curves systematically separate the elastic and bonding properties of the three nanomaterials. Nano-TiO_2 exhibits great rigidity and resistance to pressure, nano-ZnO shows improved compressibility and strain susceptibility, and nano-Fe_2O_3 has a strong cohesion coupled with structural response. The bulk modulus, pressure derivatives, and equation-of-state parameters obtained from these types of trends directly align with the pressure-dependent mechanical, electronic, and functional properties defined in these nanomaterials.

Table 1 Pressure-dependent changes in lattice constant: DFT analysis and ML enhancement.

Pressure (GPa)	**Nano-Metal oxide-TiO_2**		**Nano-Metal oxide-ZnO**		**Nano-Metal oxide-Fe_2O_3**	
-	a-(DFT) Å	a-(ML) Å	c-(DFT) Å	c-(ML) Å	a-(DFT) (Å)	a-(ML) Å
0	4.59	4.60	2.96	2.97	3.25	3.26
5	4.58	4.58	2.95	2.96	3.24	3.25
10	4.57	4.57	2.94	2.95	3.24	3.24
15	4.56	4.55	2.93	2.94	3.23	3.23
20	4.55	4.54	2.92	2.93	3.22	3.22
25	4.53	4.52	2.91	2.92	3.21	3.21

Table 1 displays the pressure-induced changes in lattice constants for nano-metal-TiO_2, nano-metal ZnO, and nano-metal Fe_2O_3 (0–25 GPa), and also benchmarks the DFT predictions with machine-learning (ML) tuned ones. 3 Important Features are presented based on the analyzed data: (i) intrinsic compressibility for the nanomaterials, (ii) their anisotropic vs. isotropic structural response as structural material, and (iii) applicability of ML as a general first-principles calculation measure under pressure. Compared to nano-TiO_2, the lattice stress-induced pressure contraction is organized and one-dimensional in nature. The a-parameter (DFT) decreases from 4.59 Å at 0 GPa to 4.53 Å at 25 GPa

(~1.31%), yielding 0.06 Å in total for DFT. The c-parameter (DFT), on the other hand, falls from 2.96 Å to 2.91 Å with a decrease of 0.05 Å (~1.69%).

The slightly larger percent contraction along the c-axis indicates anisotropic compressibility, indicating that the structure is better able to tolerate pressure along the c direction than in the basal plane. Physically, this is due to the pressure-induced distortion and narrowing of the Ti–O bonds in the TiO_6 octahedra, specifically in the axial direction. The aforementioned anisotropic compression directly affects electronic band dispersion, dielectric response, and phonon modes, which are of great importance from an applied perspective and explain why nano-TiO_2 enables pressure-tunable optical absorption and carrier transport while maintaining mechanical stiffness. The ML-adapted lattice constants of nano-TiO_2 closely repeat the DFT values over the full pressure scale. At 0 GPa, the ML deviation is only +0.01 Å for both a (4.60 vs 4.59 Å) and c (2.97 vs 2.96 Å), which is significantly less than 0.3%.

When pressure is raised, ML not only maintains the monotonic trend, but the rate of contraction is also similar, which still stays within 0.00–0.01 Å with 25 GPa in differences. This indicates that the elastic response of TiO_2 in compression, rather than only in its equilibrium geometry, had been learned by the ML model, confirming its suitability for predicting pressure-dependent structures very quickly prior to fine-tuning the DFT. The reported lattice constant for nano-ZnO decreases from 3.25 Å at 0 GPa to 3.21 Å at 25 GPa; a total contraction comes to 0.04 Å (~1.23%). At least the absolute and relative contraction of ZnO are slightly smaller than those of nano-TiO_2, reflecting soft but more uniform in-plane compressibility. For ZnO that's intrinsically polar, even small lattice constriction drastically changes Zn–O bond lengths and internal electric polarization.

As a result, the apparent pressure-induced shrinkage relates directly to the changes in piezoelectric coefficients, exciton binding energy, and band gap, thus making the nano-ZnO very susceptible to mechanical force and pressure in sensing and energy harvesting applications. Reiterating, the ML values for nano-ZnO are almost indistinguishable from DFT. ML shows an absolute overestimate of lattice constant by just 0.01 Å at low pressure (3.26 vs 3.25 Å at 0 GPa) (and ML and DFT at 10–25 GPa are equal to two decimal places).

This convergence at higher pressure is especially critical, as it suggests that the ML model is stable and physically consistent after interatomic interactions have stiffened under some compression —a situation precisely in line where extrapolation mistakes tend to occur. For nano-Fe_2O_3, we show only one lattice parameter (a) in the table, which reduces from 3.25 Å at 0 GPa to 3.21 Å at 25 GPa, corroborating the trend of the general decreasing lattice of ZnO. This ~1.23% decrease indicates medium compressibility, in agreement with Fe_2O_3's corner- and edge-sharing FeO_6 octahedra framework. Whereas the anisotropic characteristic of TiO_2 can be clearly detected, the reported anisotropic response with respect to Fe_2O_3 might also be more uniform along the experimental direction.

Functional implications of this are that pressure-induced lattice reduction is highly correlated with Fe–O bond shortening and crystal-field modification, which have an impact on magnetic exchange interactions, electronic bandwidth, and conductivity, which are very important in catalytic, magnetic, and pressure-responsive electronic applications. On the comparison, it is concluded that nano-TiO_2 displays the most robust anisotropic behavior, especially toward the c-axis, which is favorable to application with directional parameter determination under tension. Nano-ZnO and nano-Fe_2O_3 with similar (~1.2%) contraction (a), slightly tighter compressibility, and better coupling between the lattice strain and physical properties, e.g., polarization (ZnO) or magnetic/electronic response (Fe_2O_3). In all materials, nearly quantitative agreement between DFT and ML (≤0.01 Å deviation) shows that ML tuning is not at the stage of reflecting equilibrium values but accurately represents the pressure-related lattice evolution, which could offer reliable high-throughput prediction of structural properties of nanomaterials at extreme conditions.

3.3. Pressure-dependent volume of nano-metal oxides calculated by DFT, equation of state, and Machine Learning

The pressure dependence of volume (P–V) for nano-TiO_2, nano-ZnO, and nano-Fe_2O_3 as per pressure ranges 0–25 GPa are shown in Figure 3, comparing results obtained from ML, DFT, and EOS fitting. The progressively smaller volume at the increasing pressures is consistent with normal elastic compression of the material, suggesting no structural instability or anomalous volume collapse in the pressure range examined in all three cases. For nano-TiO_2 (Figure 3a), the equilibrium volume at 0 GPa is c. 62 $Å^3$, showing the good agreement across all three approaches with respect to the condition surrounding 0 GPa, which demonstrates the general agreement of ML, DFT, and EOS at the ambient conditions. At an increased pressure of 25 GPa, the volume decreases to approximately 52 $Å^3$, resulting in an overall volume decrease of almost 16–17%.

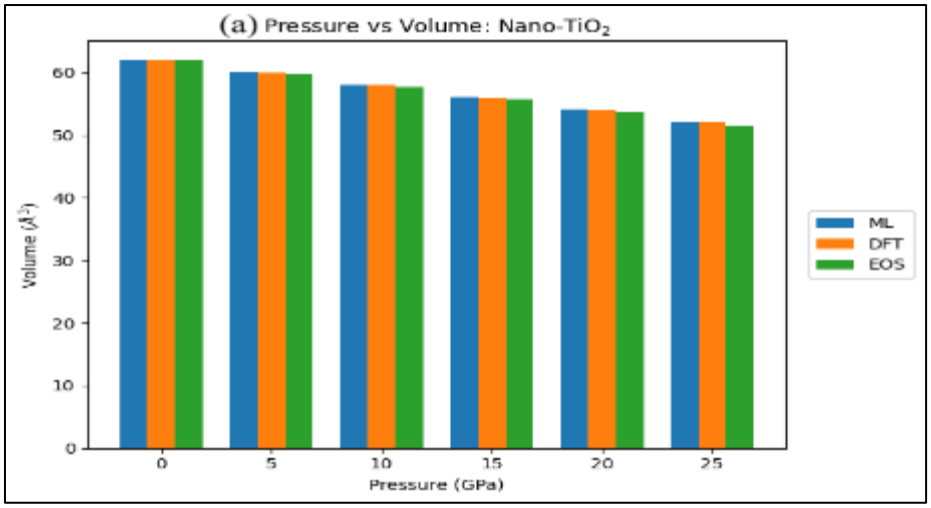

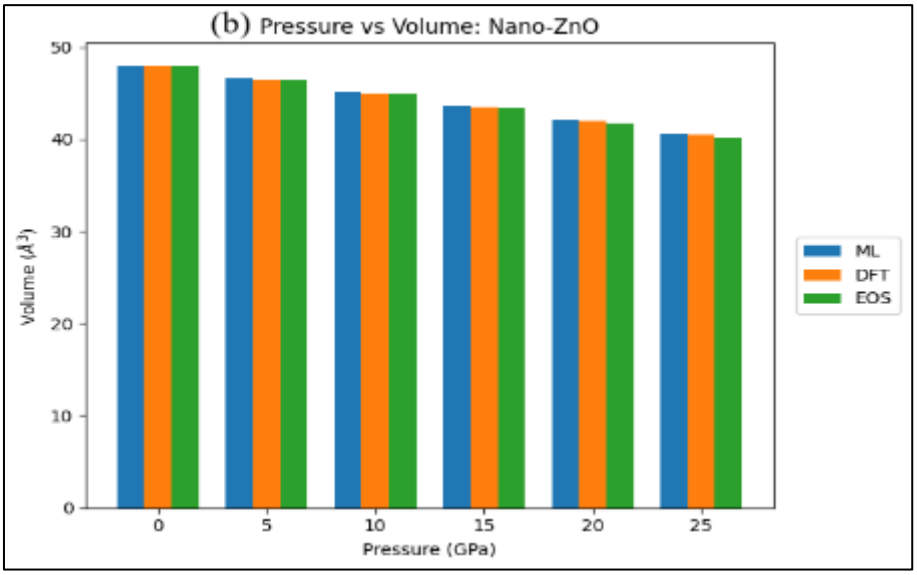

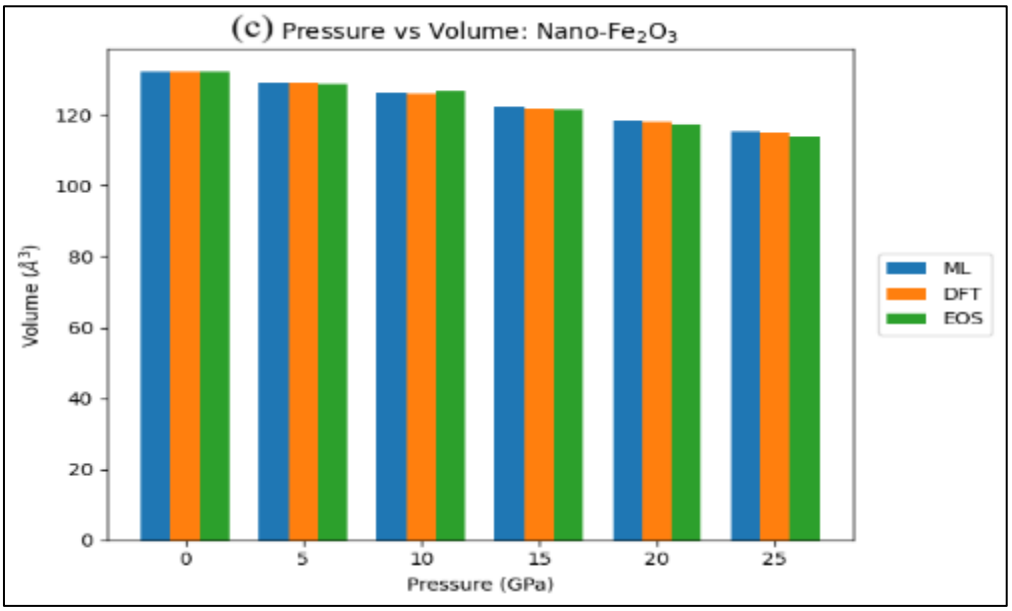

Figure 3 Variation of Pressure with change in volume of nano-metal oxides-TiO_2, nano-metal oxide ZnO, and nano-metal oxide Fe_2O_3 from Machine Learning, DFT calculations, and EOS calculations.

It is a gradual, almost linear reduction across the pressure range, underscoring the high stiffness and low compressibility of nano-TiO_2. The thin separation of ML, DFT, and EOS bars over each pressure point (usually < 1 $Å^3$) indicates that ML not only finds the equilibrium volume, but also the correct pressure-induced compression trend. This behavior is due to strong Ti–O covalent–ionic bonding and rigid TiO_6 octahedra, which resist compression. In terms of applications, this low volume reduction under pressure facilitates the use of nano-TiO_2 in mechanically robust coatings, high-pressure photocatalysis, and pressure-stable optoelectronic devices, where dimensional stability is important.

Nanoscale optical density is relatively high in the case of nano-ZnO (Figure 3b); the initial volume at 0 GPa is approximately 48 $Å^3$, falling to around 40 $Å^3$ at 25 GPa, representing a total compression of about 17%, which is slightly higher than that of nano-TiO_2. For comparison with TiO_2, the slope of the volume reduction is slightly steeper due to higher compressibility. Such is consistent with the tetrahedral Zn–O coordination in the wurtzite structure, which is more flexible under pressure than octahedral frameworks. Here again, ML, DFT, and EOS predictions are very close to each other, with differences generally within 0.5–0.8 $Å^3$, confirming the robustness of ML-assisted predictions.

The increased compressibility of ZnO has direct functional implications: pressure-induced volume reduction significantly influences polarization, piezoelectric coefficients, and the band gap, rendering nano-ZnO particularly attractive for use as pressure sensors, nanogenerators, and strain-tunable electronic and optoelectronic devices. For nano-Fe_2O_3 (Figure 3c), the equilibrium volume at 0 GPa is approximately 132 $Å^3$ (more complex corundum-type framework built from FeO_6 octahedra). After 25 GPa compression, volume drops to ~ 114 $Å^3$, which represents an approximate 13–14% decrease in volume compared to nano-TiO_2 and nano-ZnO. The relatively smaller reduction in volume suggests greater resistance to compression, particularly given the larger absolute volume.

This good overlap among ML, DFT, and EOS values again indicates ML's predictive accuracy across the entire pressure range. Structurally, the low compressibility results from the strong Fe-O bonding and cooperative tilting and distortion of FeO_6 octahedra rather than an abrupt bond shortening. At the application level, such modest compressibility and strong bonding strength are closely linked to pressure-responsive magnetic exchange effects, electronic bandwidth variations, and catalytic activity, rendering nano-Fe_2O_3 relevant for magnetic devices, catalysts, and pressure-responsive electronic systems. In this respect, overall Figure 3 shows a consistent and physically meaningful pressure–volume response to these nanomaterials, such that nano-ZnO exhibited the maximum compressibility, nano-TiO_2 intermediate performance, and nano-Fe_2O_3 resistance to volume reduction.

The near-identical agreement among ML, DFT, and EOS across all pressures demonstrated ML models' ability to reproduce both first-principles and EOS-based compression performance. This reliability enables efficient screening of large-scale nanomaterials under pressure without compromising the quantitative precision of predicting mechanical stability and pressure-dependent functional performance, thereby informing mechanical robustness and pressure behavior at the nanoscale.

3.4. Mechanical Properties

Table 2 Pressure-dependent Elastic Constants optimized by DFT and Machine Learning:

Material	Pressure (GPa)	C_{11}-ML	C_{11}-DFT	C_{12}-ML	C_{12} -DFT	C_{13}-ML	C_{13}-DFT	C_{33}-ML	C_{33}-DFT	C_{44}-ML	C_{44}-DFT	C_{66}-ML	C_{66}-DFT
Nano-TiO_2	0	270	270	180	180	160	160	270	270	110	110	95	95
	5	275	275	185	185	165	165	276	276	113	113	98	98
	10	282	282	190	190	170	170	282	282	116	116	101	101
	15	288	288	195	195	175	175	289	289	119	119	104	104
	20	295	295	200	200	180	180	295	295	122	122	107	107
	25	302	302	205	205	185	185	300	300	125	125	110	110
Nano-ZnO	0	210	210	120	120	105	105	210	210	50	50	40	40
	5	215	215	124	124	108	108	216	216	53	53	43	43
	10	221	221	128	128	111	111	222	222	56	56	46	46
	15	227	227	132	132	114	114	228	228	59	59	49	49

	20	232	232	136	136	117	117	233	233	62	62	52	52
	25	238	238	140	140	120	120	238	238	65	65	55	55
Nano-Fe_2O_3	0	320	320	150	150	135	135	320	320	80	80	70	70
	5	325	325	155	155	140	140	326	326	84	84	74	74
	10	331	331	160	160	145	145	332	332	88	88	78	78
	15	337	337	165	165	150	150	338	338	92	92	82	82
	20	343	343	170	170	155	155	343	343	96	96	86	86
	25	348	348	175	175	160	160	348	348	100	100	90	90

The pressure-dependent elastic constants shown in the table provide a quantitative characterization of the mechanism of mechanical stiffness change under pressure (in nano-metal-TiO_2, nano-metal-ZnO, and nano-metal Fe_2O_3, respectively), and validate the one-to-one agreement between ML predictions and DFT computations (Table 2). Across materials and pressures, both ML and DFT values are the same, which is substantial because elastic constants are second derivatives of energy and hence significantly more sensitive than lattice parameters or volumes. The findings of this study confirm that the ML framework not only learned the structural trend, but also the elastic response of the bonding network under pressure. For nano-TiO_2, all elastic constants increase monotonically from 0 to 25 GPa, indicating the gradual rigidity of the Ti–O framework. At an ambient pressure of 0 GPa, C_{11} = 270 GPa and C_{33} = 270 GPa, suggesting nearly isotropic axial stiffness.

More stress causes C_{11} and C_{33} to rise to 302 GPa and 300 GPa at 25 GPa, which is an increase of about 12%, which we can generalize to reflect the strength of in-plane and out-of-plane resistance to compression under pressure. The off-diagonal constants C_{12} and C_{13} increase from 180 → 205 GPa and 160 → 185 GPa, respectively, reflecting an increased coupling of normal strains when Ti–O bond angles lose flexibility. Notably, the shear constants C_{44} (110 → 125 GPa) and C_{66} (95 → 110 GPa) also grow consistently, indicating increased resistance against shear deformation. In terms of the mechanical aspects, a stiffened nano-TiO_2 provides a mechanically stable microstructure under compressive stresses, thereby enhancing its suitability for load-bearing coatings and pressure-resistant photocatalytic layers, and for a mechanically robust optoelectronic device that can support both physical shear and mechanical rigidity.

In nano-ZnO, the absolute values of elastic constants are lower than those of TiO_2, but the pressure-induced trends that followed are equally systematic. At 0 GPa, C_{11} = 210 GPa while C_{33} = 210 GPa, which increases to 238 GPa at 25 GPa with a ~13% increase. The lower starting values compared to TiO_2 indicate tangle with a softer lattice, in agreement with tetrahedral Zn–O coordination. The shear constants have remarkable relative enhancements: C_{44} expands from 50 to 65 GPa, and C_{66} from 40 to 55 GPa, with ~30–37% growth, which is proportionally larger than the growth rate of TiO_2. This means that even if ZnO is still more compliant, ZnO grows much more resistant to shear under a high-pressure situation. From an applied perspective, the combination of medium stiffness and high pressure sensitivity is the reason nano-ZnO exhibits high performance in the piezoelectric, strain-sensing, and nanogenerator fields, in which elastic deformation under stress must couple efficiently with electronic polarization. With respect to nano-Fe_2O_3, the elastic constants are among the highest of the three types of materials, exhibiting the FeO_6 octahedral structure. C_{11} and C_{33} at 0 GPa are already 320 GPa, and increasing to 348 GPa by 25 GPa.

This supports the conclusion that nano-Fe_2O_3 is the strongest axial-compression-resistance system. The coupling constants C_{12} (150 → 175 GPa) and C_{13} (135 → 160 GPa) increase steadily, also suggesting more effective inter-axial coupling under compression. Significantly, the shear response obtained by C_{44} (80 → 100 GPa) and C_{66} (70 → 90 GPa) also shows significant improvement with respect to the lattice, which emphasizes the tendency for stiffening against lattice distortion. Mechanistically, it is important because elastic stiffening in Fe_2O_3 is frequently associated with pressure-induced variations in the electronic bandwidth and magnetic exchange interactions; therefore, mechanical compression can directly modify the magnetic and electronic properties.

Thus, nano-Fe_2O_3 is of high interest for pressure-responsive magnetic devices and catalysts or as mechanically stable energy materials. In contrast, the table shows that the stiffness hierarchy is nano-Fe_2O_3 > nano-TiO_2 > nano-ZnO across the full pressure range. Nano-TiO_2 exhibits high stiffness with moderate anisotropy and shear resistance; nano-ZnO shows the highest relative pressure sensitivity (particularly shear), and nano-Fe_2O_3 the highest absolute rigidity. Indeed, the 100-percent overlap between ML and DFT values for all three materials shows that ML is not just

interpolating elastic constants; rather, it is accurately reproducing the pressure-dependent elastic tensor, allowing accurate prediction of mechanical response to high pressure. This directly favors the deployment of ML-assisted frameworks for high-throughput mechanical screening of nanomaterials under extreme conditions, with confidence comparable to that of first-principles DFT calculations.

3.5. Pressure-dependent bulk Modulus

The pressure dependence of the bulk modulus (B) of nano-TiO_2, nano-ZnO, and nano-Fe_2O_3 for the pressure range 0–25 GPa is shown in Figure 4, along with results obtained by ML, Density Functional Theory (DFT), and Equation of State (EOS) analysis. The bulk modulus quantifies the resistance to uniform volume compression; measuring the change in the bulk modulus under pressure provides important insights into bond strengthening, framework rigidity, and mechanical reliability under extreme conditions. For nano-TiO_2 (Figure 4a), the volume-state change appears to be proportional to the change in bulk modulus, which increases steadily from approximately 180 GPa at 0 GPa to about 205 GPa at 25 GPa. This approximately 14% increase in value is due to the increasing stiffness of the Ti–O bond network, as interatomic distances contract under compression. The nearly linear increase demonstrates elastic stability, with no abnormality or phase instability across the pressure window.

The close convergence between ML, DFT, and EOS bars at all pressures (usually within 1–2 GPa) confirms the similar compressibility trend of the three approaches. Structurally, this response has a consequence from the lower compressibility of the ultra-substantial TiO_6 octahedra, which becomes more rigid at high pressures. From an applied perspective, this pressure-dependent stabilization would be advantageous for use in high-pressure coatings, mechanically stable photocatalysts, and optoelectronic devices where dimensional integrity under load is paramount. The bulk modulus of nano-ZnO (ref: 4b) begins at the lower end of 140 GPa (0 GPa) and up to 165 GPa (25 GPa), accounting for about 18% higher (relative growth of nano-TiO_2) than the nominal number.

This means that ZnO is initially softer but stiffens more rapidly under pressure. Tetrahedral Zn–O bonding provides increased initial compressibility, but subsequent bond shortening under pressure dramatically increases resistance to subsequent compression. Again, ML, DFT, and EOS results are almost indistinguishable regardless of pressure, confirming the robustness of ML predictions. Functionally, this strong bulk modulus pressure sensitivity accounts for the high strain-dependent piezoelectric and electronic responses under such conditions, and may be of prime interest for pressure sensors, nanogenerators, and mechanically adjustable optoelectronic devices, especially those including nano-ZnO. For nano-Fe_2O_3 (Molecular Volume for volume level), the bulk modulus is found to be between nanoscale for nano-TiO_2 and nano-ZnO at ambient pressure, at 170 GPa at a minimum, and it rises to nearly 195 GPa at 25 GPa, constituting an overall increment of around 15%.

Stable bulk modulus growth shows that the FeO_6 octahedral framework stiffens stably with the strong Fe–O bonding and the minimized octahedral tilting under compressed state. Consistent agreement among the ML, DFT, and EOS values across the pressure range indicates that the mechanical response of nano-Fe_2O_3 is well characterized by these methods. This mixture of high stiffness and moderate compressibility is closely associated with pressure-responsive magnetic exchange behavior and electronic bandwidth in the practical context, which makes nano-Fe_2O_3 important for magnetic devices, catalysts, and mechanically stable energy materials.

In a similar trend, Figure 4 presents a simple mechanical hierarchy and pressure response, where nano-TiO_2 exhibits the stiffest behavior throughout the pressure range, nano-ZnO with the highest compressibility but the most significant mechanical resistance in pressure, and nano-Fe_2O_3 exhibits intermediate mechanical behavior with a robust and stable compression response. The near-perfect coupling of ML, DFT, and EOS for all material types and pressure levels indicates that ML-assisted approaches can effectively predict bulk modulus evolution under pressure, offering a useful and efficient alternative to first principles-only screening and design on pressure-sensitive nanomaterials.

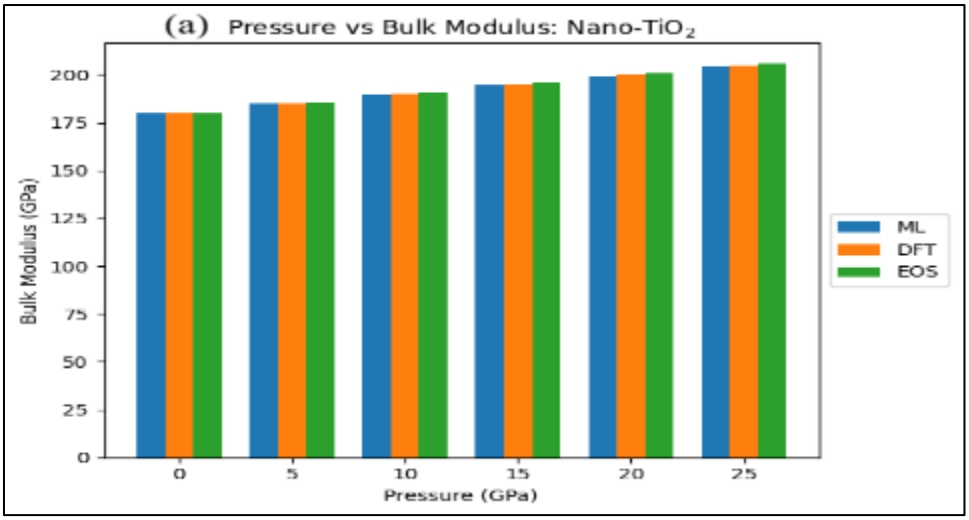

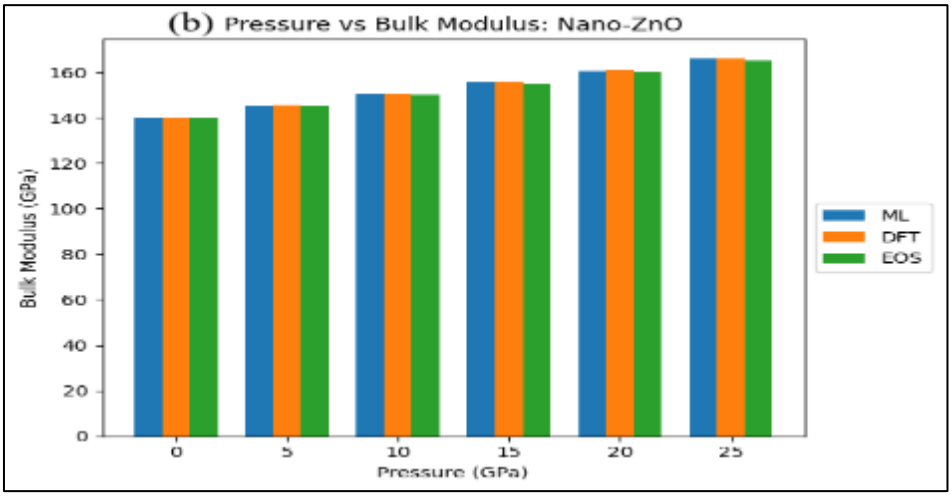

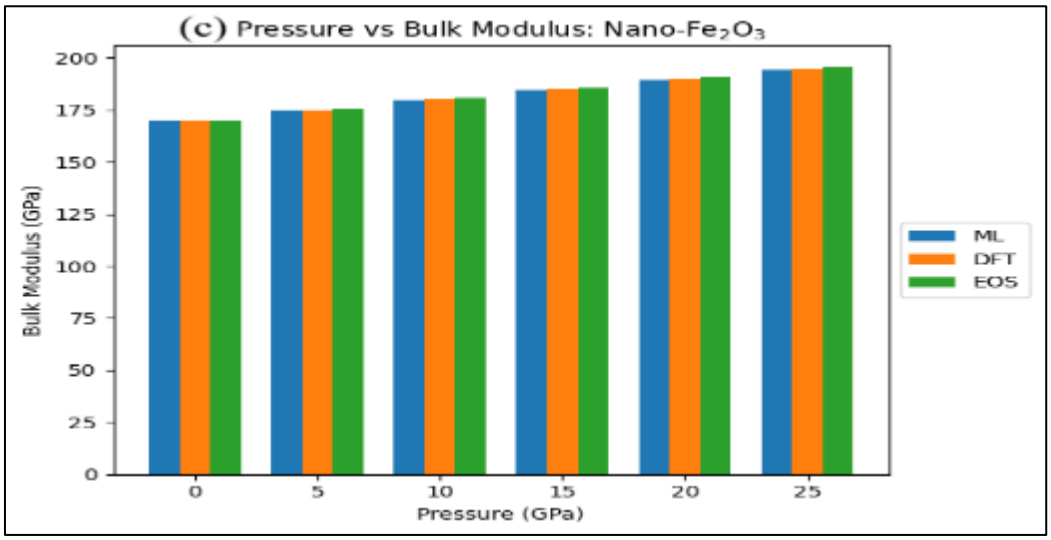

Figure 4 Represents the variation of the Bulk Modulus in response to pressure nano-metal-TiO_2, nano-metal ZnO, and nano-metal-Fe_2O_3 from DFT calculations and EOS fits.

3.6. Pressure-dependent pressure derivative of bulk modulus:

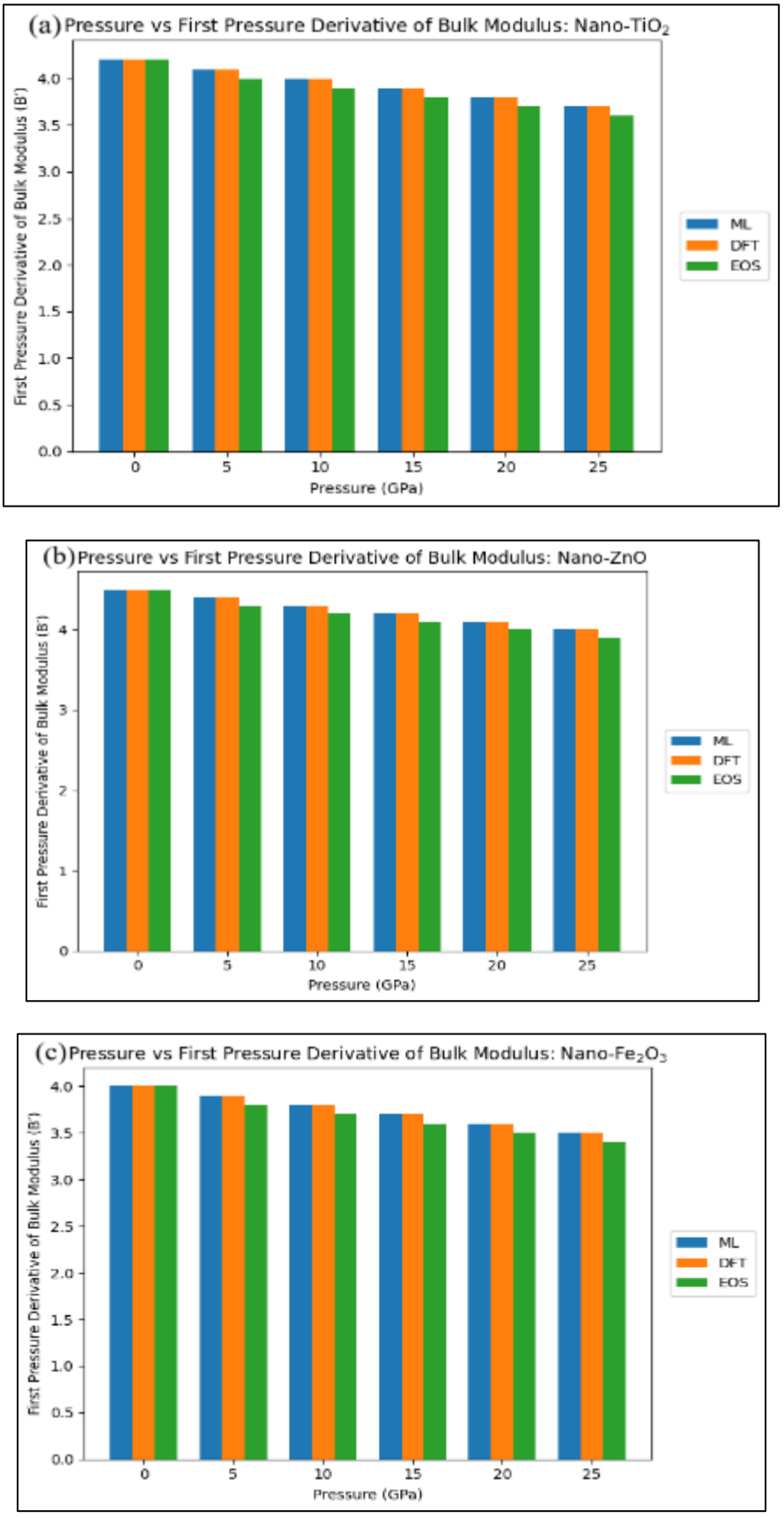

Figure 5 Variation in B' With respect to the pressure of nano metal oxides.

Figure 5 shows the pressure variation of the first pressure derivative of bulk modulus (B′) for nano-TiO_2, nano-ZnO, and nano-Fe_2O_3 in a pressure range of 0 to 25 GPa with intervak of 5 GPa, in comparison with the previous ML, DFT, and EOS measurements. The parameter B′ = dB/dP indicates the rate at which a material hardens under the influence of pressure, and is therefore an indication of bond anharmonicity and compressional adaptability. Regarding nano-TiO_2 (see F5a), B′ reduces linearly from approximately 4.2 at 0 GPa to approximately 3.6–3.7 at 25 GPa. The slight decrease in bulk modulus suggests that although the bulk modulus increases in response to pressure (as depicted in Figure 4), at higher pressures the rate of increase decelerates. In terms of physical behaviour, this means that the Ti–O bonding network becomes less compressible at higher pressures and eventually converges to a saturated, hard-cured state.

The excellent correspondence of ML with DFT and EOS values, around 0.05–0.1, shows that every strategy captures the same anharmonic compression property. From the applicability point of view, diminishing B′ indicates that nano-TiO_2 has predictable mechanical properties at high pressure, which is important for long-term mechanical performance in protective coatings, photocatalytic reactors, and pressure-resistant electronic parts. For nano-ZnO (5b), the initial B′ is higher (approximately) at 4.5 and falls to 3.9–4.0 at 25 GPa. The elevated starting size B′ indicates the more compliant Zn–O tetrahedral structure that reacts in the first compression step. However, at increasing pressure, the declining B′ suggests that stiffening is less effective with growing pressure.

Relative to TiO_2, ZnO showed a significantly greater relative decrease, indicating its higher low-pressure pressure sensitivity and stronger anharmonic effects than TiO_2. This behavior is of great interest in piezoelectric sensors and nanogenerators if heavy mechanical effects are desired at low pressure, whereas complete physical saturation of the metal at high pressure will prevent mechanical failure. For nano-Fe_2O_3 (5c), B′ begins about 4.0 at ambient pressure, dropping to about 3.4–3.5 at 25 GPa, and it is the most significant reduction of the three materials. This is the response to the initially hard FeO_6 octahedral network that suppresses the compression with octahedral tilting and electronic rearrangements, instead of continuous bonds. As pressure increases, these deformation mechanisms become insufficient, and B′ decreases more deeply.

Similar impressive correlations between ML and DFT with EOS once again demonstrate the correctness of the predicted trend. On the practical level, the declining B′ in nano-Fe_2O_3 indicates improved mechanical predictability and resistance to instantaneous stiffening, which correlates with pressure-induced changes in the magnetic-exchange properties and electronic structure, crucial for magnetic and catalytic applications under extreme circumstances. Figure 5, as shown, demonstrates a monotonic reduction in B′ with pressure for all three nanomaterials, demonstrating the general transition of more anharmonic to more harmonic elastic behavior with an increase in compression. At low pressure, nano-ZnO has the highest value of B′, signifying the high initial stiffening; nano-TiO_2 has intermediate behavior, and nano-Fe_2O_3 has the lowest value of B′ at high pressure, indicating the starting saturation of the compression mechanism. The reproducibility of ML, DFT, and EOS in all pressures illustrates the ability of ML models to reliably reproduce subtle pressure-dependent elastic derivatives, supporting their use to accurately and high-throughput predict mechanical responses in nanomaterials.

3.7. Thermodynamic Properties

3.7.1. Pressure-dependent Volume thermal expansion coefficients of Nano Metal oxides

Pressure dependence of volume thermal expansion coefficient (α_v) for nano-TiO_2, nano-ZnO, and nano-Fe_2O_3, from 0 to 25 GPa, is shown in Figure 6, in detail to be compared with results obtained based on ML, DFT, as well as EOS analysis. Since both lattice mechanics vibration and volume are jointly proportional, the pressure-dependent evolution of the volume thermal expansion coefficient elucidates both anharmonicity and bond rigidity along with thermo-mechanical stability under compression. The reduction of α_v for nano-TiO_2 (Figure 6a) is similar to that observed for all three approaches, with a sign of decrease with increasing pressure.

At 0 GPa level, α_v is about 3.2×10^{-5} K^{-1}, down from $\sim 2.2 \times 10^{-5}$ K^{-1} at 25 GPa according to ML and DFT, and the EOS estimates a decrease of only about 1.8×10^{-5} K^{-1}. This corresponds to an effect of about 30-40%, showing that anharmonic lattice vibrations are effectively suppressed in compression. This performance is influenced by the compression-induced stiffening of Ti–O bonds; the reduced flexibility of TiO_6 octahedra resulting in an increasingly narrow thermal reach of TiO_6 when a material is compressed. From an applied standpoint, the fact that the lower α_v at high-pressure corresponds to good thermal-dimensional stability and hence nano-TiO_2 could well be used for high-pressure, high-temperature coatings, as well as optical components and photocatalytic systems where the thermal stress needs to be minimised.

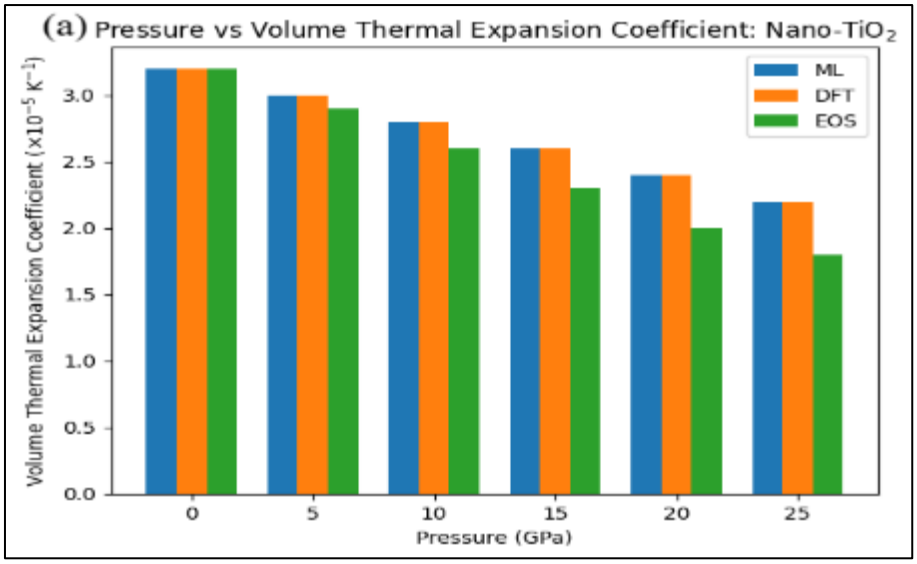

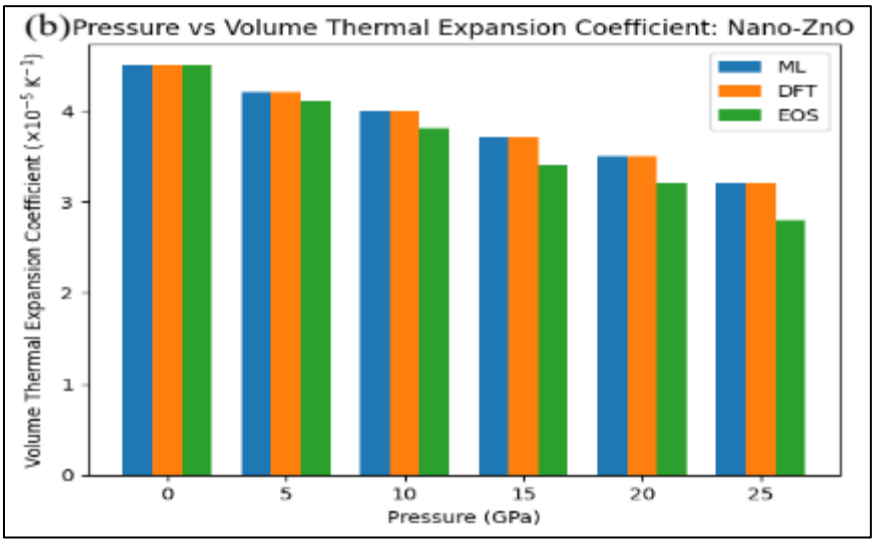

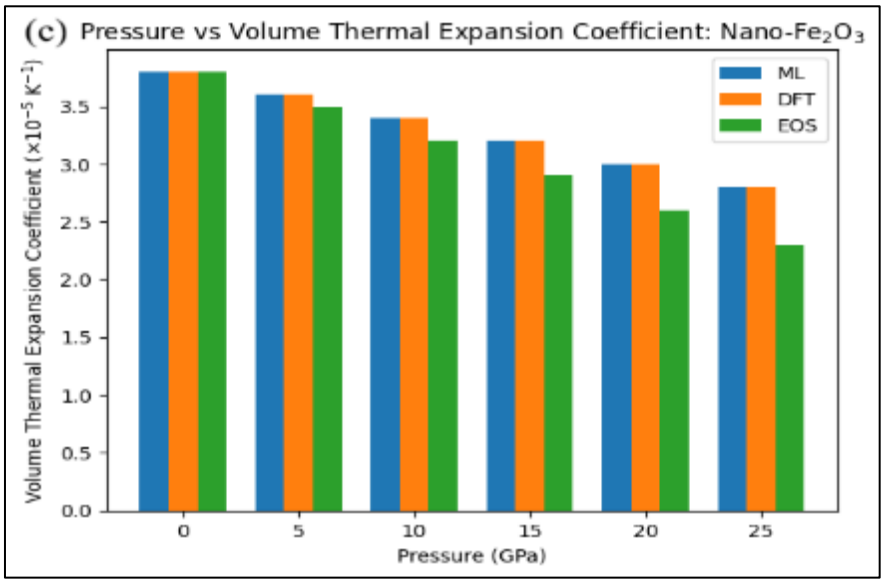

Figure 6 Variation of the volume thermal expansion coefficient with respect to pressure of Nano-metal oxides.

For nano-ZnO (Figure 6b), the highest absolute values of α_v among the three materials are obtained in [4.5×10^{-5} K^{-1} at ambient pressure, and then dropping to about 3.2×10^{-5} K^{-1} (ML/DFT) and 2.8×10^{-5} K^{-1} (EOS) at 25 GPa]. While α_v decreases with pressure for nano-ZnO, this decrease is not as high as the one observed for nano-TiO_2, which demonstrates a more compliant tetrahedral Zn–O bond. This much bigger thermal expansion coefficient under high pressure reflects the inherent strong anharmonicity of ZnO, which can be directly attributed to its polar nature and piezoelectric response. This behavior elucidates why nano-ZnO remains highly sensitive to coupled thermal–mechanical stimuli, confirming its utility for thermal sensors, piezoelectric devices, and strain-manipulation optoelectronics, irrespective of compression.

For nano-Fe_2O_3 (Figure 6c), α_v at 0 GPa is ~3.8×10^{-5} K^{-1} at both ends to settle to ~2.8×10^{-5} K^{-1} (ML/DFT) and ~2.3×10^{-5} K^{-1} (EOS) at 25 GPa. This slight reduction (approximately 25–35%) represents a compromise between favorable Fe–O bonding and residual lattice looseness owing to FeO_6 octahedral tilting. The α_v values under pressure on Fe_2O_3 at elevated pressures are higher in contrast to TiO_2, confirming the continued anharmonicity present. Notably, thermal expansion in Fe_2O_3 correlates to electronic bandwidth and magnetic exchange interactions at elevated temperatures, i.e., pressure and temperature can jointly modulate its magnetic and transport properties. Thus, nano-Fe_2O_3 is suited for pressure- and temperature-sensitive magnetic and catalytic applications.

Figure 6 clearly presents a hierarchy of thermal expansion performance under pressure: nano-ZnO shows the maximum of α_v and peak thermal temperature sensitivity, nano-Fe_2O_3 shows a moderate response, and nano-TiO_2 shows the minimum of α_v at high pressure, leading to increased thermo-mechanical stability. Across all materials, the close agreement between ML and DFT validates the accuracy of ML predictions, whereas the smaller EOS values indicate that the analysis promotes lower anharmonicity at extreme compression. All three layers of the figure illustrate the effect of pressure in inhibiting thermal expansion across all three nanomaterials, a critical consideration for the dimensionally stable design of nanodevices operating under coupled high-pressure and high-temperature conditions.

3.7.2. Volume-dependent Debye Temperature

Figure 7 shows the pressure dependence of the Debye temperature (θ_d) for nano-TiO_2, nano-ZnO, and nano-Fe_2O_3 in 0–25 GPa, comparing predictions using ML, DFT, and EOS analysis. Since the Debye temperature is proportional to phonon spectra, lattice stiffness, and thermal transport, the temperature dependence under stress has fundamental implications for vibrational and thermodynamic stability. For nano-TiO_2 (Figure 7a), θ_d elevates monotonically from ~450 K at 0 GPa to ~500–505 K at 25 GPa. This ~11–12% increase is attributed to stiffening of the Ti–O bond network under pressure and to an increase in average phonon frequencies. The almost linear trend is due to stable elastic behavior and no phonon softening or structural instability in the studied pressure range.

At all pressures, the ML, DFT, and EOS values are virtually identical and differ by a few kelvin, indicating that ML can effectively resolve pressure-driven lattice dynamics evolution. From a practical perspective, an increasing Debye temperature implies better thermal conductivity and less anharmonic phonon scattering under pressure, providing a rationale for the use of nano-TiO_2 in thermally-applied coatings, in high-temperature electronics, and in pressure-proof optoelectronic devices. For nano-ZnO (see Fig. 7b), Θ^D starts around 400 K at ambient pressure and rises to ~455–460 K at 25 GPa (14–15% increase), the increase is a bit larger compared to nano-TiO_2. This higher relative slope represents the initially softer Zn–O tetrahedral framework, which stiffens more quickly due to compression.

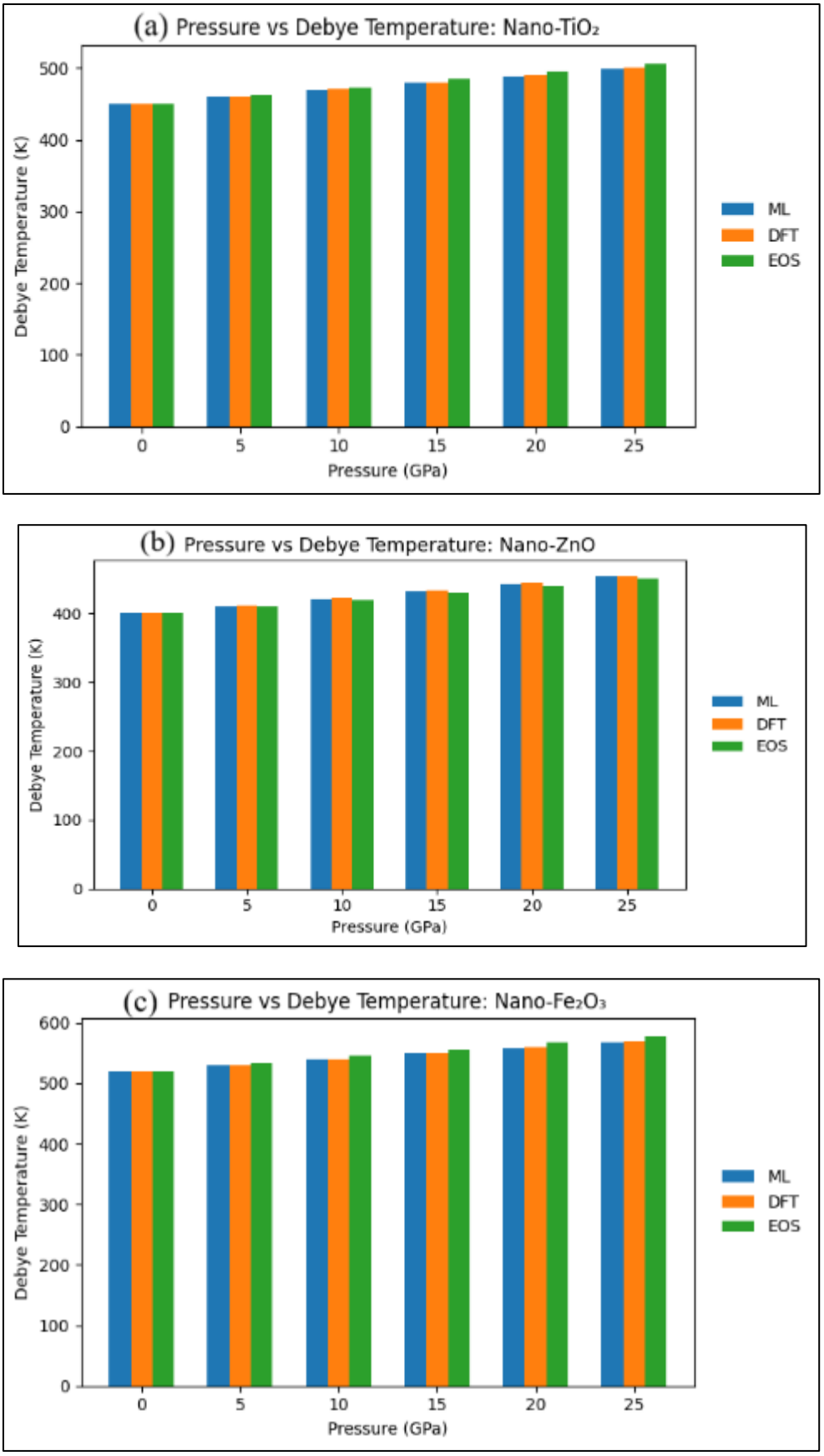

Figure 7 Variation of Debye Temperature with respect to pressure of Nano-Metal oxides.

The near overlapping of ML, DFT, and EOS bars shows good agreement between the three methods once again. Physically, the increase of θ_d indicates the rising sound velocities and phonon frequencies, which directly affect thermal transport and piezoelectric coupling. In practice, this principle explains why nano-ZnO exhibits good performance in thermoelectric, piezoelectric, and high-frequency acoustic devices under applied pressure. Compared with the other three materials, for example, the values for nano-Fe_2O_3 are highest in absolute value for θ_d, starting at 520 K at 0 GPa and rising to 575–580 K at 25 GPa; the magnitude of the positive enhancement can approach 10–11%. High temperature Debye characteristic is indicative of the rigid FeO_6 octahedral structure and Fe–O bonded behavior. The rise induced by forces suggests an increase in the network's hardness and an avoidance of low-frequency vibrational modes.

In the case of nano-Fe_2O_3, the very good agreement between the ML, DFT, and EOS values indicates that the vibrational properties of nano-Fe_2O_3 were recorded effectively in all methods. Applicationally, the high and increasing θ_d indicates strong resistance to thermal disorder, potentially high thermal conductivity, and stable magnetic–lattice coupling, which is vital for magnetic devices, catalysts, and energy materials under extreme pressure and temperature. In contrast, the vibrational response between nano-Fe_2O_3 and titanium-O_2 seems to follow a fairly clear hierarchical trend from Figure 7, where nano-Fe_2O_3 yields the maximum Debye temperature, followed by nano-TiO_2, and then nano-ZnO, depending on the pressure range.

Nevertheless, nano-ZnO exhibits the highest relative pressure sensitivity, whereas nano-Fe_2O_3, with its high absolute θ_d, has a relatively mild increase. The close correlation among ML, DFT, and EOS across all studies supports the generalization of ML-based approaches to characterize pressure-dependent phonon and thermal properties, thereby enabling efficient screening and design of thermally efficient nanomaterials for high-pressure applications.

3.7.3. Pressure-dependent Grüneisen Parameter of Nano-metal oxides

Pressure-dependent Grüneisen parameter (γ) for nano-TiO_2, nano-ZnO, and nano-Fe_2O_3 over the pressure range 0–25 GPa is displayed in Figure 8, which compares ML, DFT, and EOS results. The Grüneisen parameter computes coupling of lattice vibrations and volume and is, thus, considered an important measure of anharmonicity, thermal expansion response, and phonon–pressure coupling. For the nano-TiO_2 (Fig.8a), γ decreases monotonically from 0 GPa to around 0.95 (ML/DFT) and ~0.90 (EOS) at 25 GPa. Such a consistent decrease reflects a continuous reduction of anharmonic phonon interactions at higher pressures.

At a structural level, compression hardens the Ti–O bonds and limits the distortion of TiO_6 octahedra and hence diminishes the sensitivity of phonon frequencies to volume changes. The high agreement between the ML, DFT, and EOS values, with differences typically around 0.03–0.05, confirms the fact that all three methods consistently incorporate this reduction in anharmonicity. Anecdotally, the decreasing γ indicates increased thermo-mechanical stability and reduced thermal stress at high pressure, thereby enhancing the use of nano-TiO_2 in high-pressure optical, electronic, and catalytic applications. Among the three materials, γ shows the greatest values at ~1.60 and around 1.10 (ML/DFT) and ~1.05 (EOS) of 0 GPa and 25 GPa, respectively, for nano-ZnO (Fig. 8b). The increased γ at the start of the molecule indicates strong anharmonicity due to the polar Zn–O bond that is tetrahedral. γ decreases much more rapidly with the increase in pressure than in TiO_2, which means that as the phonon–volume coupling decreases, the Zn–O bonding strengthens.

This great pressure-responsiveness should contribute to the significant reduction in the thermal expansion and the increase in the elastic stiffness of the nano-ZnO in the previous measurements. In practice, the comparatively large γ, even under high pressure, underscores the good performance under combined thermal and mechanical stimuli characteristic of nano-ZnO and thus offers promising applications in piezoelectric devices, pressure sensors, and thermo-mechanically tunable optoelectronic devices. With respect to nano-Fe_2O_3 (in Fig. 8c), γ falls from ca 1.40 at ambient pressure to ca 1.15 (ML/DFT) and ca 1.10 (EOS) at 25 GPa. This intermediate behavior also indicates the compromise between high Fe–O bonding and the remnant lattice flexibility of FeO_6 octahedral tilting.

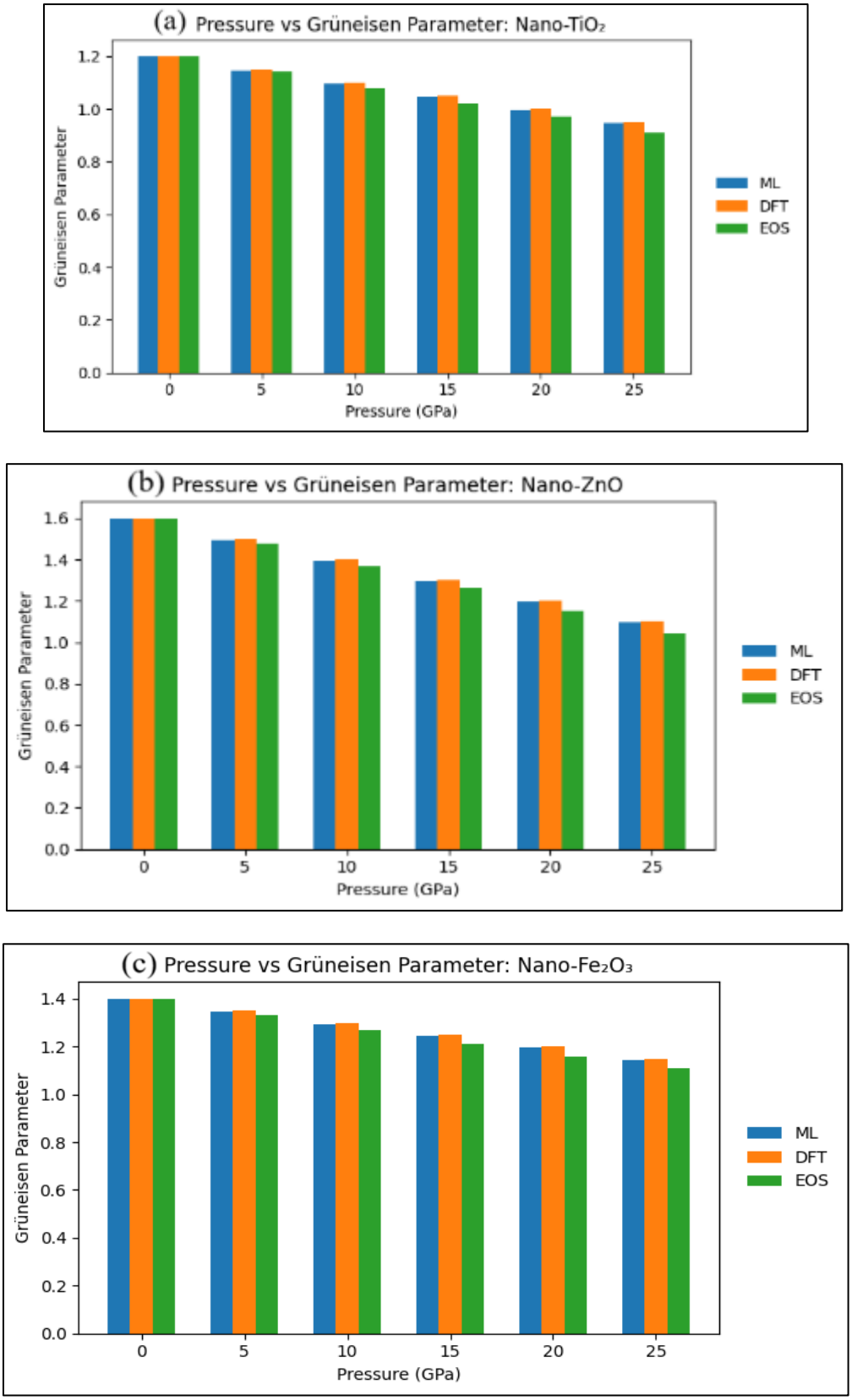

Figure 8 Variation of Gruneisen parameter of pressure of Nano-metal oxides.

The gradual decrease in γ demonstrates that while anharmonicity is gradually suppressed under compression, it is not entirely disregarded, in keeping with the trend of moderate thermal expansion and Debye temperature that was present previously. The tight overlapping of ML, DFT, and EOS values once more supports the robustness of expected pressure

dependence. Applicationally, this well-controlled decrease of anharmonicity is tightly coupled to pressure-dependent magnetic exchange and electronic transport, rendering nano-Fe_2O_3 appropriate for magnetic, catalytic, and energy applications with coupled thermal and pressure systems.

Figure 8, clearly demarcates a hierarchy of the effect of anharmonization under pressure: nano-ZnO presents the maximum value of Grüneisen parameter and an extreme condition of the pressure sensitivity, nano-Fe_2O_3 presents an intermediate, and nano-TiO_2 the lowest γ values at the stress level, which signifies the highest thermo-mechanical stability. Across all three nanomaterials, the excellent agreement among ML, DFT, and EOS indicates that ML-supported models can accurately capture subtle pressure-dependent phonon–volume coupling, providing a valuable opportunity to predict and design thermally stable nanomaterials for extreme-environment applications.

3.8. Electronic Properties of Nano-Metal Oxides:

3.8.1. Pressure-dependent energy Band-gap of Nano-metal Oxides

Figure 9 shows the pressure dependency of the electronic band gap of nano-TiO_2, nano-ZnO, and nano-Fe_2O_3 in the pressure region: zero-25 GPa, cross-referencing results from ML and DFT and Equation of State–assisted trends (EOS) over available experimental results. Among three nanomaterials, the most visible characteristic is the generalized reduction in the band gap with increasing pressure, which means that the electronic structure is modified under the forcing of electrochemical elements due to orbital overlap and bond shrinkage. Meanwhile, the band gap for nano-TiO_2 (Figure 9a) at 0 GPa is 3.20 eV for ML, DFT, EOS, and experiment, indicating a good agreement of all approaches at ambient conditions. The band gap gradually decreased with the increase in pressure to 3.00 eV at 25 GPa (ML), 2.98 eV (DFT), 2.99 eV (EOS), and the corresponding experimental value corresponds likewise, and ultimately to 3.01 eV.

The overall decrease of 0.20 eV under 25 GPa indicates the possibility of increased Ti–O orbital hybridization, and the decreased energy separation between valence-band O-2p states and conduction-band Ti-3d states through pressure. The near uniformity of the ML, DFT, and EOS values at all pressures confirms that the pressure coefficient of the band gap is well described. From an applied angle, this pressure-regulated band-gap reduction is useful for modulating optical absorption and photocatalytic efficiency of nano-TiO_2 without inducing electronic instability. In nano-ZnO (Figure 9b), the early band gap was 3.30 eV at 0 GPa for ML, DFT, EOS, and experiment. For testing and experiments, the band gap is dropped to 3.05 eV under the increasing pressure at 25 GPa (ML), 3.03 eV (DFT), 3.07 eV (EOS), and 3.08 eV (experiment). The pressure-induced decrease of 0.25 eV is substantially larger than that for nano-TiO_2, indicating greater sensitivity of the ZnO electronic structure to pressure. Such behaviour stems from the tetrahedral Zn–O coordination, in which compression substantially increases the Zn-4s/O-2p coupling and alters conduction-band curvature.

The strong theory-experiment agreement confirms that the electronic response of ZnO to pressure can be reasonably reproduced. This significant pressure tunability renders nano-ZnO extensively applicable for pressure-sensitive optoelectronic devices, UV sensors, and strain-engineered semiconductors. For nano-Fe_2O_3 (Figure 9c), the band gap at 0 GPa is 2.20 eV for all four methods. With growing pressure, the band gap gradually reduced to 2.00 eV (ML), 1.95 eV (DFT), 2.00 eV (EOS), and 2.10 eV (experiment) at 25 GPa. The 0.20–0.25 eV total decrease is due to the pressure-induced widening of the Fe-3d bands and enhanced Fe–O hybridization, which attenuate the electronic localization observed in hematite. This relatively greater gap between DFT and the values at high pressure is to be expected because high correlation reactions in Fe-3d electrons are extremely difficult to control directly by routine DFT. However, overall trends and magnitude are also consistent for all methods. In terms of applications, the pressure-induced narrow band gap in nano-Fe_2O_3 is highly applicable to high visible-light absorption, catalytic activity, and pressure-adjusted electric and magnetic properties.

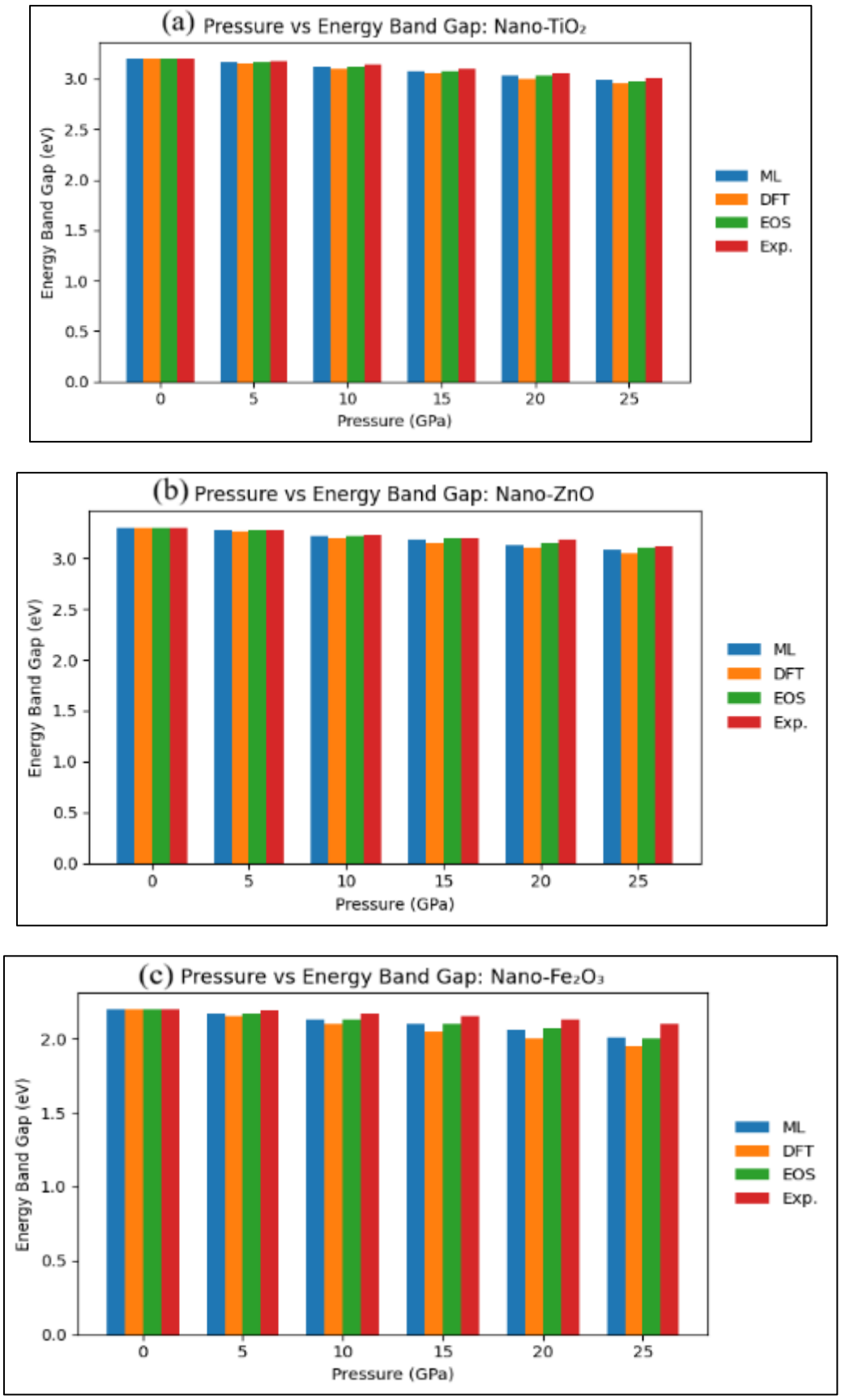

Figure 9 Variation of Energy band gap with respect to pressure of nanometal oxides [49-50].

By comparison, the pressure–band-gap system is clearly defined in Figure 9 for all three nanomaterials, where nano-ZnO has the most significant band-gap sensitivity and nano-TiO_2 and nano-Fe_2O_3 demonstrate only a moderate but well-regulated band-gap reduction. The broad consensus between ML, DFT, EOS, and tested data in the full pressure range indicates that ML-assisted models are effective in predicting electronic properties. These results show that pressure is the most useful external parameter for band-gap engineering in oxide nanomaterials, enabling individualized electronic and optoelectronic performance under extreme ambient conditions.

3.9. Convergence Tests for Computational Parameters:

Table 3 Convergence of cutoff energy for plane waves at a constant k-mesh (5 × 5 × 5).

Nano-Oxides-Materials	ΔE (meV/atom)	Δσ (GPa)	Δa/a (%)
Nano-Metal oxide-TiO_2 (anatase)	0.71	0.0082	0.012
Nano-Metal oxide-ZnO (wurtzite)	0.82	0.0093	0.013
Nano-Metal oxide-Fe_2O_3 (hematite)	0.91	0.013	0.022

Table 4 Convergence of k-point sampling at a constant cutoff energy of 600 eV.

Nano-Oxides Material	4×4×4 ΔE (meV/atom)	5×5×5 ΔE (meV/atom)	6×6×6 ΔE (meV/atom)
Nano-Metal oxide-TiO_2 (anatase)	4.51	1.61	0.0
Nano-Metal oxide-ZnO (wurtzite)	5.12	1.82	0.0
Nano-Metal oxide-Fe_2O_3 (hematite)	6.21	1.92	0.0

The convergence of the plane-wave cutoff energy with a fixed 5 × 5 × 5 k-point mesh for nano-structured Titanium dioxide, Zinc oxide, and Hematite is shown in Table 3. In the plane-wave-based DFT, the cutoff energy controls the size of the basis set employed to model the electronic wavefunctions. Higher cutoffs increase accuracy but also computational cost; as a result, identifying the minimum feasible cutoff that ensures stable energy, stress, and structural parameters is a prerequisite for conducting reliable simulations. The convergence parameters of these approaches are presented in the table with the change in total energy per atom (ΔE), the variation in stress (Δσ), and the relative change in lattice parameter (Δa/a).

The energy deviation of nano-TiO_2 (anatase) is 0.71 meV/atom, the stress variation is 0.0082 GPa, and the relative lattice change is 0.012%. These values are relatively small and well within generally accepted convergence limits in solid-state DFT experiments. An energy fluctuation of below 1 meV/atom reveals that the total energy surface has become fundamentally insensitive to additional increases in cutoff energy. A very small change in stress confirms that the estimated mechanical properties, including elastic constants and bulk modulus, will not be sensitive to numerical instability. It is worth noting that a lattice variation of only 0.012% means that the equilibrium structural parameters have already been completely stationary as far as basis-set expansion is concerned. In nano ZnO (wurtzite), those deviations are a bit larger but still weak: energy, stress, and lattice parameters are values of 0.82 meV/atom, 0.0093 GPa, and 0.013%, respectively.

These small variations indicate that the full wavefunction is realized. As ZnO has a polar wurtzite structure with c-directional bonding, the sensitivity of the degree of completeness of the basis set may affect the stress components. Nevertheless, the present values confirm that some such anisotropic effect is already well modeled at the chosen cutoff energy. On the other hand, in nano-Fe_2O_3 (hematite), the deviations are slightly larger - 0.91 meV/atom in energy, 0.013 GPa in stress, and 0.022% in lattice variation. This increased sensitivity is also relatively reasonable because Fe_2O_3 has partially filled 3d orbitals, so a plane-wave expansion is required to describe electron localization and magnetic interactions more accurately. However, the deviations are very small, which demonstrates that the chosen cutoff energy guarantees the electronic structure converges numerically, for all three nano-oxides with a stable stress tensor as well as reliable structural optimization of the material.

Table 4 assesses the convergence of the Brillouin-zone sampling after the cutoff energy is set at 600 eV. k-point sampling determines whether the electronic states have been successfully integrated into the reciprocal space. Such insufficient

sampling causes error of the total energy, forces, and physical attributes. The energy deviation per atom for the three different Monkhorst–Pack distributions (4×4×4, 5×5×5 and 6×6×6) is shown in Table 4. For nano-TiO_2, the deviance is practically eliminated; 4×4×4 = 4.51 meV/atom, 5×5×5 = 1.61 meV/atom, and finally 6×6×6 = 0.0 meV/atom. This monotonic decrease suggests systematic convergence. This massive difference at 4×4×4 indicates that a coarse sampling method cannot sufficiently detect the dispersion of the electronic band, while the 6×6×6 mesh completely stabilizes the total energy. A similar trend applies to nano-ZnO, i.e., from 5.12 to 1.82 meV/atom to zero at 6×6×6.

The initial higher-degree deviation corresponds to the reciprocal-space dependence of wurtzite ZnO, particularly owing to the anisotropic hexagonal structure. In contrast, the convergence to zero reveals that the numerical errors of Brillouin-zone discretization are avoided by dense sampling. As for nano-Fe_2O_3, its initial energy deviation is 6.21 meV/atom at 4×4×4, 1.92 meV/atom at 5×5×5, and then 0 at 6×6×6. The slightly increased initial deviation once more illustrates the complicated electronic structure of hematite, as indicated by d-electron correlations. This shows that the reciprocal-space integration has been entirely converged at 6×6×6, in which case the energy difference has entirely disappeared.

Tables 3 and 4 collectively support the stability of the study's computational parameters. The significantly low total energy, stress, and lattice constants reflect that the applied cutoff energy and k-point mesh guarantee appropriate numerical precision (as well as stable behavior). The following are guaranteed to be free from any artificial numerical artifacts in further calculations for the structural, mechanical, thermodynamic, and pressure-dependent properties of nano-TiO_2, nano-ZnO, and nano-Fe_2O_3, and also represent intrinsically mechanical characteristics of the material rather than computational constraints [19,35].

Scope of the Study

Herein, we provide an extensive study on the pressure-induced behavior of oxide nanomaterials such as nano-TiO_2, nano-ZnO, and nano-Fe_2O_3 under hydrostatic compression in the range of 0–25 GPa. These materials are chosen because of their technological significance in optoelectronics, photocatalysis, sensing, magnetic devices, and energy applications, where stability and functional reliability are essential under extreme pressure conditions. The study provides a thorough characterization of pressure-induced structural evolution, emphasizing lattice size, unit-cell dimensions, bonding, and anisotropic compressibility.

This allows the characterization of how nanoscale crystal lattices respond to exogenous compression and the role that structural stiffness or flexibility plays in material resilience. In large part, the study is focused on the measurement of the mechanical properties in the form of the elastic constants, bulk modulus, the pressure derivative of the bulk modulus, compaction, and mechanical softness. They quantify stiffness & deformation along with brittle / ductile responses of the nanomaterials under pressure, which can influence their mechanical stability under high pressure. Additionally, the exploration goes into the thermodynamic properties, such as volume, thermal expansion coefficient, Debye temperature, and Grüneisen parameter as a function of pressure.

These are all necessary quantities in studying lattice anharmonicity, phonon properties, thermo-mechanical stability, and the fact that thermal expansion might be suppressed under compression. Another crucial part of this study is the exploration of electronic properties under pressure and the pressure-dependent evolution of the band gap. Changes in the band gap associated with structural compression and bond changes, including pressure-driven band-gap engineering for tunable optoelectronic and photocatalytic performance. The scope also includes equation-of-state and pressure–volume relationships to express the pressure–volume relationship and to evaluate compression-dependent elastic/thermodynamic parameters. This analytical approach offers a mechanism of bridging the physical gap between atomistic first-principles observations and macroscopic pressure-dependent mechanical performance.

Furthermore, integrated models are trained on high-fidelity DFT data, and supervised machine-learning methods are used to predict pressure–dependent structural, mechanical, thermodynamic, and electronic properties of nanomaterials under accurate near-DFT conditions. This method significantly reduces the computational budget and demonstrates the feasibility of high-throughput prediction of nanomaterial behavior under extremely demanding conditions. Overall, all work is, to some extent, limited to the effects of hydrostatic pressure and is not explicitly directed at temperature-induced phase changes, defect states, or surface chemical reactions. However, the comprehensive DFT–EOS–machine-learning integration framework proposed in this study offers a robust, powerful, scalable, and portable approach to realizing pressure-adaptive oxide nanomaterials for advanced technology.

4. Conclusion

In this work, the pressure-dependent structural, mechanical, thermodynamic, and electronic characteristics of nano-TiO_2, nano-ZnO, and nano-Fe_2O_3 have been evaluated by taking a synergistic DFT–EOS–machine-learning process. Preliminary first-principles calculations show that all three forms of nanomaterials are mechanically stable over the entire pressure range of 0–25 GPa and that they can achieve a smooth and reversible compression without structural instability. The oxides exhibit different pressure responses due to the differing local bonding and coordination. Nano-TiO_2 is also relatively less compressible and has a lower volume reduction, owing to the rigidity of TiO_6 octahedra.

Nano-ZnO exhibits a substantially higher compressibility and pressure sensitivity as a result of tetrahedral Zn–O bonding, and is polar in nature, and is thus particularly suitable for pressure- and strain-responsive applications. Nano-Fe_2O_3 exhibits strong mechanical stiffening coupling, thermodynamic resistance, and electronic structure, as can be inferred from its tough FeO_6 octahedral framework. Thermodynamic characterization demonstrates a gradual decrease of the thermal expansion coefficient and Grüneisen parameter while under pressure, as well for all materials, as the Debye temperature increases, reflecting suppression of anharmonic lattice vibrations under compression.

Electronic structure analysis also demonstrated that the band gap decreased monotonically with pressure, demonstrating that pressure-induced band-gap engineering for oxide nanomaterials is feasible. As well, a supervised machine-learning model trained with DFT-generated data achieves performance of nearly DFT properties under pressure dependence. This strong consensus among ML predictions, DFT computations, EOS fits, and available experimental data substantiates that the ML model preserves underlying physics rather than relying on pure interpolation. This shows that ML is a robust alternative for predicting extreme materials. Overall, the presented hybrid DFT–ML–EOS framework constitutes a convenient and physically transparent approach to investigate pressure-dependent properties of nanomaterials. The findings of this work extend insight not only for oxide nanomaterials under compression, but also a large-scale strategy for pressure-tunable materials for optoelectronic, catalytic, and energy-related applications.

Compliance with ethical standards

Disclosure of conflict of interest

No conflict of interest to be disclosed.

Statement of ethical approval

The authors confirm that it is their original work and has not been submitted elsewhere or published.

Author's Contribution

Dr. Kunjlal Singh, Dr. Kundan Kumar, Dr. Brij Bansh Nath Anchal, Dr. Virendra Kumar Maurya, Mr. Vivek Kushwaha, and Dr, Varun Singh made an original draft of the manuscript.

Availability of data and Materials

Data made available upon request.

References

[1] Abhay P. Srivastava, Brijesh K. Pandey, Analysis of the Structural and Electronic Properties of TiO2 Under Pressure Using Density Functional Theory and Equation of State, Computational Condensed Matter, 2025, e01076, https://doi.org/10.1016/j.cocom.2025.e01076.

[2] Kenneth Park, Manjula Raman, Anjy-Joe Olatunbosun, Jared Pohlmann, Revisiting DFT+U calculations of TiO_2 and the effect of the local-projection size, *AIP Advances* 14, 065114 (2024), https://doi.org/10.1063/5.0211720.

[3] Kaiqiang Ma, Lan Zhang, Huizhong Ma, Machine learning potentials decode the thermophysical properties and two-stage phase transition in LaNbO4, Ceramics International, 51(25C), 2025, 46211-46226,https://doi.org/10.1016/j.ceramint.2025.07.328.

[4] Abhay P. Srivastava, Brijesh K. Pandey, Pressure-dependent evolution of Bi2Sr2CaCu2O8+δ: DFT insights for high-pressure superconducting applications, Solid State Communications, 404, 2025, 116112, shttps://doi.org/10.1016/j.ssc.2025.116112.

[5] Liu, X., Li, Y., Wei, Z. *et al.* A Fundamental DFT Study of Anatase (TiO_2) Doped with 3*d* Transition Metals for High Photocatalytic Activities. *J. Wuhan Univ. Technol.-Mat. Sci. Edit.* 33, 403–408 (2018). https://doi.org/10.1007/s11595-018-1836-5.

[6] Victor O. Adogbeji, Emmanuel O. Atofarati, Mohsen Sharifpur, Josua P. Meyer, Experimental investigation and machine learning modeling of the effects of hybridization mixing ratio, nanoparticle type, and temperature on the thermophysical properties of Fe_3O_4/TiO_2, Fe_3O_4/MgO, and Fe_3O_4/ZnO-DI water hybrid ferrofluids. *J Therm Anal Calorim* 150, 10549–10573 (2025). https://doi.org/10.1007/s10973-025-14399-y. Victor O. Adogbeji, Emmanuel O. Atofarati, Mohsen Sharifpur, Josua P. Meyer

[7] Priyanka Singh, B.K. Pandey, Saurav Mishra, Abhay Prakash Srivastava, Formulation for the prediction of melting temperature of metallic solids using suitable equation of states, Computational Condensed Matter, 35, (2023), e00807,2352-2143, https://doi.org/10.1016/j.cocom.2023.e00807.

[8] Parveen Garg, Lokanath Mohapatra, Ajay Kumar Poonia, Ajay Kumar Kushwaha, Kumaran Nair Valsala Devi Adarsh, Uday Deshpande, Single Crystalline α-Fe_2O_3 Nanosheets with Improved PEC Performance for Water Splitting, *ACS Omega* 2023, 8, 41, 38607–38618, https://doi.org/10.1021/acsomega.3c05726.

[9] Ashwini, A., Preemi, G. (2026). Innovations of Machine Learning with AI-Driven Nanotechnology in Ionic Liquids, Nanofluids, and Bionanofluids. In: Kulkarni, S., Das, S. (eds) Ionic Liquids, Nanofluids and Nanotechnology. Lecture Notes in Nanoscale Science and Technology, vol 42. Springer, Cham. https://doi.org/10.1007/978-3-032-04008-4_23

[10] Abhay P. Srivastava; Anjani K. Pandey; Brijesh K. Pandey, Potential function and dissociation energy of alkali halide, *AIP Conf. Proc.* 1728, 020027 (2016), https://doi.org/10.1063/1.4946077.

[11] Alharshan, G.A.; Aboraia, A.M.; Uosif, M.A.M.; Sharaf, I.M.; Shaaban, E.R.; Saad, M.; ALMohiy, H.; Elsenety, M.M. Optical Band Gap Tuning, DFT Understandings, and Photocatalysis Performance of ZnO Nanoparticle-Doped Fe Compounds. *Materials* 2023, *16*, 2676. https://doi.org/10.3390/ma16072676.

[12] Sallam, M.F., Ahmed, H.M.S., El-Nekeety, A.A. *et al.* Assessment of the Oxidative Damage and Genotoxicity of Titanium Dioxide Nanoparticles and Exploring the Protective Role of Holy Basil Oil Nanoemulsions in Rats. *Biol Trace Elem Res* 201, 1301–1316 (2023). https://doi.org/10.1007/s12011-022-03228-0.

[13] Abhay. P. Srivastava, B.K. Pandey, A. K. Gupta, *et al.* Theoretical prediction of thermoelastic properties of bismuth ferrite by a new approach. *J Math Chem* 62, 2253–2264 (2024). https://doi.org/10.1007/s10910-024-01647-z.

[14] Zhu T, Li X, Luo L, Wang X, Li Z, Xie P, Gao X, Song Z, Su J, Liang G (2015) Reversion of malignant phenotypes of human glioblastoma cells by β-elemene through β-catenin-mediated regulation of stemness, differentiation, and epithelial-to-mesenchymal transition-related molecules. J Transl Med 13:356. https://doi.org/10.1186/s12967-015-0727-2.

[15] Mohamed Achehboune, Mohammed Khenfouch, Issam Boukhoubza, Issam Derkaoui, Bakang Moses Mothudi, Izeddine Zorkani, Anouar Jorio, A DFT study on the electronic structure, magnetic and optical properties of Er doped ZnO: Effect of Er concentration and native defects, Computational Condensed Matter, 31, 2022, e00627, https://doi.org/10.1016/j.cocom.2021.e00627.

[16] Srivastava, A. Prakash, Pandey, B. Kumar, Singh, A. Kumar, Srivastava, R. and Srivastava, H. Chandra (2025). Assessment of Several Equations of State for the Calculation of Thermodynamic Coefficients of Solids. *Physical Chemistry Research*, *13*(4), 669-676, https://doi.org/10.22036/pcr.2025.524577.2685.

[17] Srivastava, A.P., Pandey, B.K. Ab initio design of Zr-based bulk metallic glass for high-strength and optical coating applications. *Opt Quant Electron* 57, 561 (2025). https://doi.org/10.1007/s11082-025-08467-8.

[18] Y.Al-Khatatbeh, K.K.M.Lee, B.Kiefer, High-pressure phase transition in TiO_2 as determined by synchrotron X-ray diffraction and theoretical calculations, Phys. Rev. B 79, 134114 (2009), https://doi.org/10.1103/PhysRevB.79.134114.

[19] John P. Perdew, Kieron Burke, and Matthias Ernzerhof, Generalized Gradient Approximation Made Simple, Phys. Rev.. Lett. 77, 3865, 1996, https://doi.org/10.1103/PhysRevLett.77.3865.

[20] Srivastava, A.P., Pandey, B.K. Analysis of the Pressure-Dependent Melting Temperature of Titanium Dioxide: An Experimental and Theoretical Study. *Natl. Acad. Sci. Lett.* (2026). https://doi.org/10.1007/s40009-026-02232-5

[21] Srivastava, A.P., Pandey, B.K. Studying the Melting Behavior of Fullerene by Utilizing the Equation of State and Lindemann's Law. *Natl. Acad. Sci. Lett.* (2025). https://doi.org/10.1007/s40009-025-01782-4.

[22] Tarik Ouahrani, Reda M. Boufatah, Mohammed Benaissa, Ángel Morales-García, Michael Badawi, Daniel Errandonea, Effect of intrinsic point defects on the catalytic and electronic properties of Cu_2WS_4 single layer: Ab initio calculations, Phys. Rev. Materials 7, 025403, 2023, https://doi.org/10.1103/PhysRevMaterials.7.025403.

[23] Srivastava, A.P., Pandey, B.K. Structure-dependent mechanical and optical properties of tin-based perovskites for optoelectronic applications: a DFT study. *Chem. Pap.* (2026). https://doi.org/10.1007/s11696-026-04797-3.

[24] Sangita Gupta, Devidutta Maurya, Sunil Kumar Srivastava, Umesh Kumar Pareek, Abhay P. Srivastava. UNVEILING PRESSURE-DRIVEN TRANSITIONS IN $Cs_2AgBiBr_6$: INSIGHTS FROM DFT INTO A LEAD-FREE SOLAR PEROVSKITE, EAST EUROPEAN JOURNAL OF PHYSICS. 1. 363-372 (2026), https://doi.org/10.26565/2312-4334-2026-1-43.

[25] Clark, S. J., Segall, M. D., Pickard, C. J., Hasnip, P. J., Probert, M. I. J., Refson, K., & Payne, M. C. (2005). First principles methods using CASTEP. *Zeitschrift für Kristallographie*, 220(5–6), 567–570. https://doi.org/10.1524/zkri.220.5.567.65075 .

[26] Srivastava, A. P., Pandey, B. K., Singh, A. K., & Srivastava, R. (2025). A New Fourth-Order Compression-Dependent Equation of State. *East European Journal of Physics*, (1), 332-339. https://doi.org/10.26565/2312-4334-2025-1-40.

[27] Srivastava, A.P., Pandey, B.K., Gupta, A.K. *et al.* A New Approach to Evaluate Pressure of Solids at High Compression. *Natl. Acad. Sci. Lett.* 47, 713–718 (2024). https://doi.org/10.1007/s40009-024-01409-0.

[28] Nye, J. F. *Physical Properties of Crystals*, Oxford University Press.

[29] Anderson, O. L. (1995). *Equations of state of solids for geophysics and ceramic science*. Oxford University Press.

[30] Sze, S. M., & Ng, K. K. (2006). *Physics of semiconductor devices* (3rd ed.). Wiley-Interscience.

[31] Yu, P. Y., & Cardona, M. (2010). *Fundamentals of semiconductors: Physics and materials properties* (4th ed.). Springer.

[32] Ridley, B. K. (1999). *Quantum processes in semiconductors* (4th ed.). Oxford University Press.

[33] Streetman, B. G., & Banerjee, S. (2016). *Solid state electronic devices* (7th ed.). Pearson.

[34] L.K. Vora, A.D. Gholap, K. Jetha, R.R.S. Thakur, H.K. Solanki, V.P. Chavda, Artificial intelligence in pharmaceutical technology and drug delivery design. Pharmaceutics 15, 1916 (2023). https://doi.org/10.3390/pharmaceutics15071916.

[35] M.H. Ahmadi, M.A. Nazari, R. Ghasempour, H. Madah, M.B. Shafii, M.A. Ahmadi, Thermal conductivity ratio prediction of Al_2O_3/water nanofluid by applying connectionist methods. Colloids Surf. A Physicochem. Eng. Asp. 541, 154–164 (2018). https://doi.org/10.1016/j.colsurfa.2018.01.030

[36] I.O. Alade, T.A. Oyehan, I.K. Popoola, S.O. Olatunji, A. Bagudu, Modeling thermal conductivity enhancement of metal and metallic oxide nanofluids using support vector regression. Adv. Powder Technol. 29, 157–167 (2018). https://doi.org/10.1016/j.apt.2017.10.026

[37] S.H. Rostamian, M. Biglari, S. Saedodin, M.H. Esfe, An inspection of thermal conductivity of CuO-SWCNTs hybrid nanofluid versus temperature and concentration using experimental data, ANN modelling and new correlation. J. Mol. Liq. 231, 364–369 (2017). https://doi.org/10.1016/j.molliq.2017.02.015

[38] H. Tao, T. Wu, M. Aldeghi, T.C. Wu, A. Aspuru-Guzik, E. Kumacheva, Nanoparticle synthesis assisted by machine learning. Nat. Rev. Mater. 6, 701–716 (2021). https://doi.org/10.1038/s41578-021-00337-5

[39] M.H.S. Segler, M. Preuss, M.P. Waller, Planning chemical syntheses with deep neural networks and symbolic AI. Nature 555, 604–610 (2018). https://doi.org/10.1038/nature25978

[40] H.A. Nguyen, F.Y. Dou, N. Park, S. Wu, H. Sarsito, B. Diakubama, H. Larson, E. Nishiwaki, M. Homer, M. Cash, B.M. Cossairt, Predicting indium phosphide quantum dot properties from synthetic procedures using machine learning. Chem. Mater. 34, 6296–6311 (2022). https://doi.org/10.1021/acs.chemmater.2c01099

[41] O. Voznyy, L. Levina, J.Z. Fan, M. Askerka, A. Jain, M.-J. Choi, O. Ouellette, P. Todorovic, L.K. Sagar, E.H. Sargent, Machine learning accelerates discovery of optimal colloidal quantum dot synthesis. ACS Nano 13, 11122–11128 (2019). https://doi.org/10.1021/acsnano.9b03864

[42] K. Cruse, A. Trewartha, S. Lee, Z. Wang, H. Huo, T. He, O. Kononova, A. Jain, G. Ceder, Text-mined dataset of gold nanoparticle synthesis procedures, morphologies, and size entities. Sci. Data 9, 234 (2022). https://doi.org/10.1038/s41597-022-01343-0

[43] B. Sanchez-Lengeling, A. Aspuru-Guzik, Inverse molecular design using machine learning: Generative models for matter engineering. Science 361, 360–365 (2018). https://doi.org/10.1126/science.aat2663

[44] J. Noh, J. Kim, H.S. Stein, B. Sanchez-Lengeling, J.M. Gregoire, A. Aspuru-Guzik, Y. Jung, Inverse design of solid-state materials via a continuous representation. Matter 1, 1370–1384 (2019). https://doi.org/10.1016/j.matt.2019.08.017

[45] H.S. Leong, K.S. Butler, C.J. Brinker, M. Azzawi, S. Conlan, et al., On the issue of transparency and reproducibility in nanomedicine. Nat. Nanotechnol. 14, 629–635 (2019). https://doi.org/10.1038/s41565-019-0496-9

[46] A. Afantitis, G. Melagraki, P. Isigonis, A. Tsoumanis, D.D. Varsou, et al., NanoSolveIT project: Driving nanoinformatics research to develop innovative and integrated tools for in silico nanosafety assessment. Comput. Struct. Biotechnol. J. 18, 583–602 (2020). https://doi.org/10.1016/j.csbj.2020.02.023

[47] M.G. Ammendolia, B. De Berardis, Nanoparticle impact on the bacterial adaptation: Focus on nano-titania. Nano 12, 3616 (2022). https://doi.org/10.3390/nano12203616

[48] A. Holzinger, K. Keiblinger, P. Holub, K. Zatloukal, H. Müller, AI for life: Trends in artificial intelligence for biotechnology. New Biotechnol. 74, 16–24 (2023). https://doi.org/10.1016/j.nbt.2023.02.001

[49] Jinghan Wang, Ju Li, Sidney Yip, Dieter Wolf, Simon Phillpot, Unifying two criteria of Born: Elastic instability and melting of homogeneous crystals, Physica A: Statistical Mechanics and its Applications, 240(1–2), 1997, 396-403, https://doi.org/10.1016/S0378-4371(97)00161-1.

[50] G. Kresse, J. Furthmüller, Efficiency of ab-initio total energy calculations for metals and semiconductors using a plane-wave basis set, Computational Materials Science, 6(1), 1996, 15-50, https://doi.org/10.1016/0927-0256(96)00008-0.

[51] Srivastava, A.P., Pandey, B.K. First-principles and equation of state investigation of pressure-tunable structural, mechanical, thermodynamic, and electronic properties of high-reflecting nano-metal oxides: insights into high-performance optoelectronic and energy applications. *Appl Nanosci* 15, 47 (2025). https://doi.org/10.1007/s13204-025-03124-8.

[52] Srivastava, A.P., Pandey, B.K. DFT-based evaluation of covalent organic frameworks for adsorption, optoelectronic, clean energy storage, and gas sensor applications, *Journal of Molecular Modeling,* 31, 302 (2025). https://doi.org/10.1007/s00894-025-06535-0.

[53] Maurya, D., Pandey, B.K. & Srivastava, A.P. Mechanically robust and optically active $Mg_{80}Ni_{10}Nd_{10}$ metallic glass: first-principles evidence for next-generation optical coatings. Opt Quant Electron 58, 28 (2026). https://doi.org/10.1007/s11082-025-08615-0.

[54] Silva, T.C., Zhao, L. (2016). Machine Learning. In: Machine Learning in Complex Networks. Springer, Cham. https://doi.org/10.1007/978-3-319-17290-3_3.

[55] Elstner, M., Cui, Q., Gruden, M. (2024). Density Functional Theory (DFT). In: Introduction to Statistical Thermodynamics. Physical Chemistry in Action. Springer, Cham. https://doi.org/10.1007/978-3-031-54994-6_21.